

Ultra-Fine 3D Bioprinting of Dynamic Hyaluronic Acid Hydrogel for in Vitro Modeling

Shima Tavakoli, Aybike Kocatürkmen, Oommen P. Oommen, and Oommen P. Varghese*

3D bioprinting bridges tissue engineering and additive manufacturing, however developing bioinks with balanced biological and physical properties remains a challenge. Hyaluronic acid (HA) is a promising base material due to its biocompatibility and cell-recognition features. An HA-based bioink is designed using dynamic disulfide-crosslinking at physiological pH by modifying HA with cysteine moieties. To overcome the slow gelation kinetics typical of disulfide-crosslinked hydrogels, potassium iodide (KI) is introduced, accelerating gelation in a concentration-dependent manner. KI not only enhances gelation but also provides radical scavenging properties while maintaining hydrogel integrity. A low KI concentration (50 mM) offers more than a 3 h printing window, ensures cell viability, and facilitates the use of fine needles (32G, 108 μm inner diameter). This enables the fabrication of large (>3 cm) and complex 3D structures. Using this bioink, an osteoarthritis disease model is developed to investigate interactions between human mesenchymal stromal cells (hMSCs) and chondrocytes, demonstrating the immunomodulatory effect of hMSCs on inflammation-induced chondrocytes. Overall, the HA-based bioink addresses critical challenges in 3D bioprinting, providing a robust platform for constructing innovative in vitro models and supporting advancements in disease modeling and precision medicine.

1. Introduction

3D bioprinting represents a cutting-edge technology at the intersection of tissue engineering and additive manufacturing, aiming to create functional and biological structures. By integrating living cells into bioinks and utilizing a precision-guided deposition system, this technique enables the fabrication of complex constructs with high geometric fidelity.^[1] The 3D bioprinting allows for the precise, layer-by-layer deposition of bioinks to form implantable tissues and sophisticated biological models.^[2] This has led to its widespread application in tissue engineering fields such as skin, vasculature, nerve tissue, cartilage, and bone models.^[1,3] The ultimate aspiration of 3D bioprinting is to revolutionize regenerative medicine by enabling the rapid design and production of clinically viable tissues and organs. Additionally, it holds immense potential in the creation of realistic in vitro disease models, offering powerful tools for investigating complex disease mechanisms and therapeutic development. Moreover, 3D bioprinting provides a

versatile platform for fabricating intricate constructs with multiple cell types, allowing for the investigation of cell–cell interactions and the dynamics of the cell–biomaterial interface within a 3D matrix. These studies provide valuable insights into cellular behavior in more physiologically relevant environments, facilitating the translation of this knowledge into clinical applications.

Several studies have highlighted the profound impact of cell interactions within a 3D matrix on cellular behavior at the molecular level. For instance, in the treatment of osteoarthritis, cell-based therapies have attracted considerable attention, particularly in using mesenchymal stem/stromal cells (MSCs) in pre-clinical models for cartilage regeneration.^[4] Despite MSCs being short-lived at the target site post-administration, they continue to provide chondroprotective and immunomodulatory effects, primarily through paracrine signaling mechanisms.^[5] Furthermore, MSC-derived exosomes have been found to promote chondrocyte proliferation in a rat model of osteoarthritis by inhibiting miR-206 through lncRNA-KLF3-AS1.^[6] In another study, Maus et al. co-cultured autologous adipose-derived stem cells with chondrocytes from osteoarthritis patients in a transwell system, observing a significant reduction in hypertrophic and fibrotic markers, including MMP-13, alkaline phosphatase, Runx2, and

S. Tavakoli, O. P. Varghese
Translational Chemical Biology Group
Division of Macromolecular Chemistry
Department of Chemistry-Ångström Laboratory
Uppsala University
Uppsala SE75121, Sweden
E-mail: oommen.varghese@kemi.uu.se

A. Kocatürkmen
Division of Pharmaceutical Biosciences
Faculty of Pharmacy
University of Helsinki
Helsinki 00790, Finland

O. P. Oommen
School of Pharmacy and Pharmaceutical Sciences
Cardiff University
Cardiff CF10 3NB, UK

 The ORCID identification number(s) for the author(s) of this article can be found under <https://doi.org/10.1002/adma.202500315>

© 2025 The Author(s). Advanced Materials published by Wiley-VCH GmbH. This is an open access article under the terms of the [Creative Commons Attribution-NonCommercial](#) License, which permits use, distribution and reproduction in any medium, provided the original work is properly cited and is not used for commercial purposes.

DOI: 10.1002/adma.202500315

collagens type I, III, and VI, alongside a 40% increase in TGF- β 1 secretion.^[7] These results emphasize the importance of studying cell–cell and cell–biomaterial interface interactions to better understand the underlying mechanisms driving tissue repair and regeneration.

Despite significant advancements in the field of 3D bioprinting, the development of an ideal bioink that meets the biological, physical, and mechanical requirements remains a challenge. From a biological perspective, bioinks must exhibit biocompatibility, cytocompatibility, and bioactivity. Ideally, the bioink should i) be derived from extracellular matrix (ECM) polymers with minimal modification to retain the functionality of the biopolymer ii) possess ideal crosslinking efficiency and kinetics that provide a vast bioprinting window iii) possess optimum degradability without producing any toxic byproducts to facilitate tissue remodeling, iv) be non-inflammatory, v) create a microenvironment that mimics the natural tissue to support high cell viability, and vi) facilitate cell function and proliferation in a spatial arrangement that mirrors the target tissue.^[1] On the physical side, bioinks must possess shear-thinning properties to ensure smooth extrusion through the printhead without causing clogging. Simultaneously, the bioink must provide sufficient mechanical strength and stiffness to maintain structural integrity post-printing.^[8] Common bioinks are derived from both synthetic and natural polymers.^[9] The most studied bioink materials are gelatin methacrylate-based (GelMA), which enables UV-mediated crosslinking, and alginate-based gels, which support Ca²⁺-induced ionic crosslinking.^[10,11] While these strategies have advanced the field significantly, both UV- and Ca²⁺-based crosslinking methods present notable limitations. Photocrosslinking can introduce cytotoxic effects or even mutagenic risks due to UV exposure and often leads to anisotropic gel properties caused by uneven light penetration. Conversely, Ca²⁺-mediated ionic crosslinking lacks long-term stability in physiological conditions, as the reversible ionic bonds can degrade over time due to Ca²⁺ ion exchange, leading to gel dissolution. To address this, additional covalent crosslinking strategies are often employed to reinforce alginate-based hydrogels. Among other natural polymer options, hyaluronic acid (HA) stands out as a key component due to its presence in the ECM of various tissues.^[10] HA is recognized for its excellent biocompatibility, hydrophilicity, and its ability to regulate critical cellular behaviors and tissue functions.^[11] However, HA-based materials inherently are weak with poor mechanical strength, necessitating crosslinking strategies for their use as a bioink for 3D bioprinting.

HA hydrogels can be engineered using a variety of chemical and physical crosslinking chemistries, enabling the creation of materials with tailored physical and mechanical properties. Notably, hydrogels synthesized via dynamic crosslinking methods—such as Schiff base, oxime, hydrazone, disulfide exchange, Diels–Alder, and boronic ester reactions—demonstrate superior viscoelastic properties, making them ideal candidates for bioink development.^[11,12] These dynamic crosslinking approaches are particularly beneficial because they impart shear-thinning and self-healing characteristics to the hydrogels, protecting cells from shear stress during the extrusion process. We have recently demonstrated that through a precise composition of the crosslinking network of HA, we could develop a bioink based entirely on HA for the effective delivery of stem cells.^[13] We

employed a combination of dynamic–non-dynamic crosslinking strategies utilizing disulfide and thiazolidine linkages to create a shear-thinning and self-healing hydrogel capable of safeguarding cells from shear forces, even when extruded through smaller needle sizes.

Among the various dynamic crosslinking approaches, disulfide chemistry is specifically interesting for designing bioinks because of its ease of reaction and its unique cell-mediated effects. Disulfide-crosslinked hydrogels can be developed using a single thiol-modified polymer that crosslinks in the presence of oxidizing agents (e.g., peroxides and I₂) or at higher pH in the presence of molecular oxygen.^[14,15] These crosslinks are also degradable by reductive agents such as glutathione (GSH), which is naturally secreted by cells.^[16] Since disulfide-crosslinking chemistry is dependent on external stimuli for faster reaction kinetics, it imposes some challenges for delivering sensitive cells such as human mesenchymal stromal cells (hMSCs). One promising approach to accelerate gelation kinetics at physiological pH is the introduction of electron-withdrawing groups at the β -position of the thiol (e.g., cysteine derivative) to reduce its pK_a, as we have shown previously.^[17] Despite this advancement, the gelation time for cysteine-modified HA at physiological pH requires over 1 h, which limits its practicality for 3D bioprinting applications.^[13] Traditionally, this issue can be resolved by adding oxidizing agents such as hydrogen peroxide (H₂O₂) or molecular I₂.^[14,18,19] These methods also impart additional challenges as peroxides produce free radicals, such as H \cdot , O \cdot , and OH \cdot that not only degrade HA but also impart cellular toxicity at higher concentrations. Molecular I₂, on the other hand, has limited water solubility and therefore requires elevated temperatures or organic solvents for reactivity.^[14,19] Thus, there is a critical need to develop an alternative oxidation method to regulate gelation kinetics without adversely affecting the physical and mechanical properties of the hydrogel or inducing any cellular toxicity.

In this study, we present a novel method to develop cysteine-modified HA hydrogel for 3D bioprinting, that remains biocompatible as well as allows extrusion through the smallest needle possible. This method relies on the use of potassium iodide (KI) as a novel catalyst that allows the oxidation of cysteine thiols at physiological conditions without the need for any additional oxidizing agents. Our results demonstrate that KI not only accelerates the gelation process but also provides radical scavenging effects, a key step toward designing immunomodulatory hydrogels. This innovative approach enabled 3D bioprinting of both chondrocytes and hMSCs—either separately or in combination—using exceptionally fine needle sizes of 30G and 32G, which, to the best of our knowledge, have not been previously reported for 3D bioprinting of HA-based hydrogels. This methodology allows for the creation of highly refined structures, offering a valuable platform to study cell interactions, particularly in the context of osteoarthritis treatment.

2. Results and Discussion

2.1. Synthesis and Characterization of Cysteine-Modified HA Hydrogel

To design a self-crosslinking bioink, we envisioned employing disulfide chemistry as this reaction can be performed at

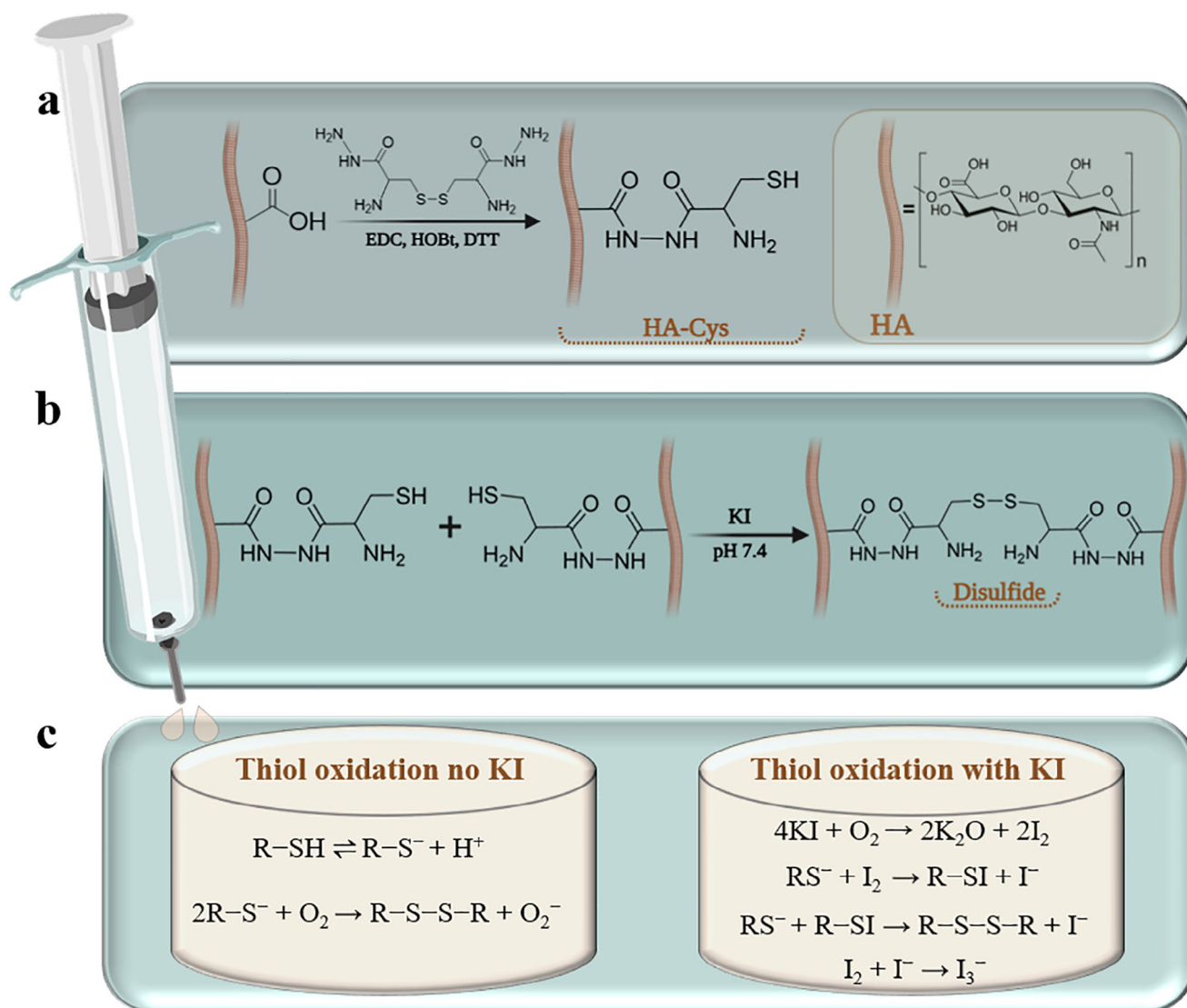


Figure 1. Schematic representation of hyaluronic acid (HA) modification and hydrogel formation. a) Modification of HA via carbodiimide coupling chemistry with cysteine hydrazide derivative. b) Formation of a hydrogel network through disulfide crosslinking in the presence of potassium iodide (KI) under physiological pH conditions. c) Detailed reaction mechanism of thiol oxidation, both in the absence and presence of KI.

physiological pH, albeit the reaction rate could be improved. In this regard, HA-modified with cysteine groups was developed. To modify HA, we employed carbodiimide coupling chemistry with *N*-hydroxybenzotriazole (HOBt) as the nucleophilic catalyst to prepare cysteine-modified HA (HA-Cys) using our previously optimized protocol using quality by design (QbD) approach (Figure 1a).^[20] We perform this reaction at pH 4.7 that allows exclusive coupling at the hydrazide terminal, keeping the amino-group free, yielding a cysteine-modified biopolymer.^[21] The degree of modification was measured by validating the ¹H NMR signals corresponding to the methine (–CHNH₂, 4.22 ppm) and methylene (–CH₂SH, 2.76 ppm) protons (Figure S1, Supporting Information). This result was further validated using Ellman's assay, which assessed the degree of chemical modification to be 10%. In this assay, 5,5'-dithio-bis-(2-nitrobenzoic acid) (DTNB) was utilized. DTNB contains an oxidizing disul-

fide bond that reacts with free thiol groups, producing 5-thio-2-nitrobenzoic acid (TNB) and a mixed disulfide as reaction products. This degree of modification was considered optimal since a lower degree could result in a weak hydrogel, whereas excessively high modification of HA may change the cell-biomaterial interactions.

The incorporation of cysteine groups onto the HA backbone is anticipated to promote disulfide bond formation under physiological conditions. Thiol groups can be oxidized in the presence of molecular oxygen (O₂) when the pH is higher than the p*K*_a of the thiol groups (Figure 1b). In HA-Cys, the presence of electron-withdrawing amino groups in cysteine at the β-position facilitates thiol group deprotonation under physiological conditions, eliminating the need for a highly basic pH.^[13,17] At physiological pH, the thiol (R–SH) is deprotonated to form a thiolate anion (R–S[–]). The thiolate anion is more nucleophilic and can react with

molecular oxygen, which may be reduced to superoxide anion (O_2^-) or other reactive oxygen species (ROS). Two thiolate anions can react directly to form a disulfide bond ($R-S-S-R$).^[22] However, this reaction is slow, with a pseudo-first-order rate constant of $k_1 = 5.04 \times 10^{-4} \text{ min}^{-1}$ at pD 7.4.^[17] To accelerate this reaction and gelation at physiological pH, various concentrations of KI were added to the hydrogel solution. The oxidation mechanism of thiol groups by KI involves a redox reaction where KI dissociates into K^+ and I^- in solution, and iodide ions (I^-) are oxidized to iodine (I_2) by losing electrons in the presence of O_2 . During the thiol oxidation reaction, the I_2 generated catalyzes the thiol group ($-SH$) oxidation to form a disulfide bond ($-S-S-$) and hydrogen iodide (HI). The hydrogen iodide (HI) can further dissociate into H^+ and I^- , which may participate in additional oxidation cycles.^[23,24] Thus, KI in the presence of oxygen facilitates the formation of disulfide bonds through a series of redox reactions at physiological pH (Figure 1c).

2.2. Influence of KI on Rheological Properties and Antioxidant Activity of HA-Cys Hydrogels

To investigate the role of KI in catalyzing thiol oxidation, we performed KI concentration-dependent gelation kinetics by time sweep measurements using a rheometer. To determine the gelling point, we measured the crossover points of storage modulus (G') and loss modulus (G'') which indicates that the material properties change from a fluid and flow-like behavior to an elastic gel-like behavior, which is considered the gelation point. As demonstrated in Figure 2a, the gelation kinetics is indeed influenced by the concentration of KI in the hydrogel solution. For instance, by the addition of 50 mM KI to HA-Cys solution, the gelation point decreased from 67.3 to 11.7 min, and at higher concentrations of KI (250 mM), the gelation time was too fast which could not be determined by rheological measurements (less than 1 min). The crossover points of G' and G'' at different KI concentrations are provided in Figures S2–S7 (Supporting Information). These results unequivocally suggest that KI can oxidize free thiol groups of HA-Cys at room temperature and physiological pH to accelerate disulfide formation in a KI concentration-dependent manner.

To further examine the effect of KI on the rheological properties of hydrogels, the G' of fully crosslinked hydrogels was measured using amplitude sweep testing. As shown in Figure 2b, the addition of KI did not significantly affect the stiffness of the gels. However, a notable decrease in G' was observed in hydrogels containing 250 mM KI. Specifically, in the HA-Cys hydrogel with 25 mM KI, G' was measured at 4005 ± 504 Pa. When the KI concentration was increased tenfold to 250 mM, the stiffness decreased to 2455 ± 684 Pa. This reduction in stiffness can be attributed to the rapid crosslinking at higher KI concentrations, which prevents homogeneous crosslinking, resulting in lower crosslinking density and diminished mechanical properties. These results are analogous to our previous studies where we demonstrated that the modulation of hydrazone and oxime crosslinking kinetics by the addition of different types of salts has profound effects on rheological properties, with faster gelation kinetics resulting in lower stiffness of the biomaterial.^[25]

In addition to its impact on gelation kinetics, KI has been reported to possess anti-inflammatory and free radical scavenging properties and therefore has been used to treat various non-infectious inflammatory skin conditions.^[26] Inflammation, along with the accumulation of ROS and free radicals, is a major contributing factor in various conditions such as chronic wounds, arthritis, and other inflammatory diseases like psoriasis and dermatitis.^[27,28] To determine the ROS scavenging activity of HA-Cys gels, both with and without KI, we performed the 2,2-diphenyl-1-picrylhydrazyl (DPPH) free radical assay. Initially, the experiment was conducted to evaluate the influence of different KI concentrations on the antioxidant properties of HA-Cys hydrogels. As illustrated in Figure 2c, the DPPH reagent showed a significant color change from deep purple to yellow with increasing KI concentrations, indicating the antioxidant effect of KI. Quantitative analysis from UV-vis spectrometry in Figure 2d revealed that HA-Cys without KI exhibited a radical scavenging activity of $44.5 \pm 3.7\%$, whereas unmodified HA showed no scavenging activity. This suggests that the thiol groups in HA-Cys can also quench the DPPH free radicals, thus functioning as an antioxidant, which corroborates with previous reports on the antioxidant properties of thiol-containing hydrogels.^[29] The incorporation of different KI concentrations into HA-Cys hydrogels led to notable changes in scavenging capacity. For example, HA-Cys containing 10 mM KI demonstrated a scavenging activity of $76 \pm 5.7\%$, which further increased to $79.8 \pm 5.1\%$ with 25 mM KI. The highest scavenging activity of $88.8 \pm 1.3\%$ was observed with the inclusion of 50 mM KI in the reaction mixture. However, further increases in KI concentration (100 and 250 mM) did not result in significant differences as compared to the 50 mM KI. These findings suggest that a KI indeed can augment the radical scavenging activity of HA-Cys hydrogels with ≈ 50 mM concentration being optimal for maximum scavenging efficiency.

2.3. Assessment of Cell Viability in HA-Cys Hydrogels with Varying KI Concentrations

To evaluate the biocompatibility of HA-Cys with different concentrations of KI, a Live/Dead assay was carried out. For this experiment, human chondrocyte cells were encapsulated within the HA-Cys hydrogels with different concentrations of KI that showed the highest scavenging activity (50, 100, and 250 mM KI). HA-Cys without KI was used as a control group. Microscopic analysis of different hydrogels with Live/Dead staining that were incubated for 1 and 3 days, is illustrated in Figure 3a. In this experiment, the green cells correspond to the live cells, whereas the red cells correspond to the dead cells. Additionally, the viability percentage of encapsulated cells was also calculated by comparing the number of live cells to the total number of cells using ImageJ software (Figure 3b). This experiment revealed that after 1 day of incubation, all the hydrogels showed high viability of cells (>90%). However, after 3 days of encapsulation, HA-Cys hydrogels without KI and with 50 mM KI showed high biocompatibility (viability >95%), while increasing the KI concentration to 100 mM reduced the viability of cells to $\approx 88\%$, indicating some level of toxicity of KI. The viability of cells was further reduced to 31% when the KI concentration was increased to 250 mM.

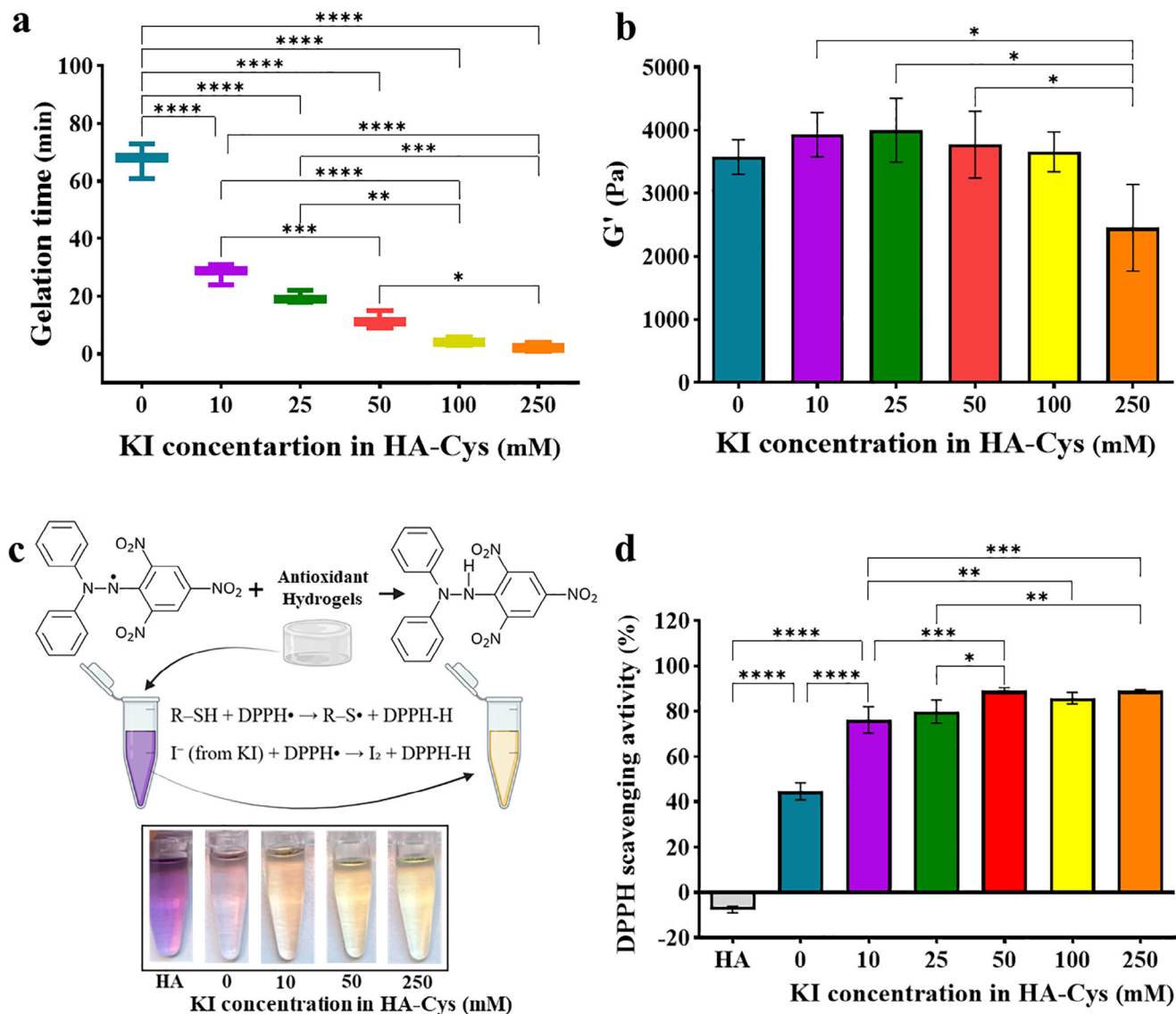


Figure 2. Influence of potassium iodide (KI) on gel formation kinetics, rheological properties, and antioxidant activity. a) Time sweep rheological measurements demonstrating the gelation point at varying concentrations of KI in cysteine-modified hyaluronic acid (HA-Cys) hydrogels. b) Effect of KI concentration on hydrogel stiffness, represented by the storage modulus (G') of the crosslinked gels. c) Schematic representation and digital images showing the reaction of hydrogels with KI and 2,2-diphenyl-1-picrylhydrazyl (DPPH). d) Quantitative data depicting the DPPH radical scavenging efficiency at different KI concentrations. Statistics: One-way ANOVA, $n = 3-5$ and significance is represented as: * = $p < 0.05$, ** = $p < 0.01$, *** = $p < 0.001$, **** = $p < 0.0001$.

To validate the biocompatibility results further, we evaluated the metabolic activity of cells using Presto Blue assay which is a resazurin-based reagent to assess cell viability and cytotoxicity. The incorporation of different concentrations of KI (50, 100, and 250 mM KI) showed no significant differences among the groups after 1 day of encapsulation (Figure 3c). However, after 3 and 7 days of encapsulation, we observed a significant reduction of metabolic activity to 39 ± 15 and $35 \pm 14\%$ respectively at high KI concentration (250 mM). Interestingly, at 50 and 100 mM KI concentrations, there were no apparent changes in the metabolic activity at these time points. Additionally, to more accurately assess the cytotoxicity of KI at concentrations lower than 250 mM, we measured the release of lactate dehydrogenase (LDH), a ubiqu-

itous enzyme found in nearly all living cells, into the media as an indicator of cell damage after 4 days of encapsulation. As anticipated, the hydrogel containing 250 mM KI exhibited the highest level of toxicity (Figure S8, Supporting Information). In contrast, the hydrogel with 50 mM KI demonstrated the lowest LDH release (20.4%), indicating minimal cell damage, even when compared to the hydrogel with 100 mM KI (33.8%). Given its minimal cytotoxicity, excellent radical scavenging properties, and significant acceleration of gelation kinetics, HA-Cys with 50 mM KI (HA-Cys.KI) was selected as the optimal formulation for further analysis.

To evaluate the effect of HA-Cys and KI on intracellular ROS levels, we induced oxidative stress in human chondrocytes by

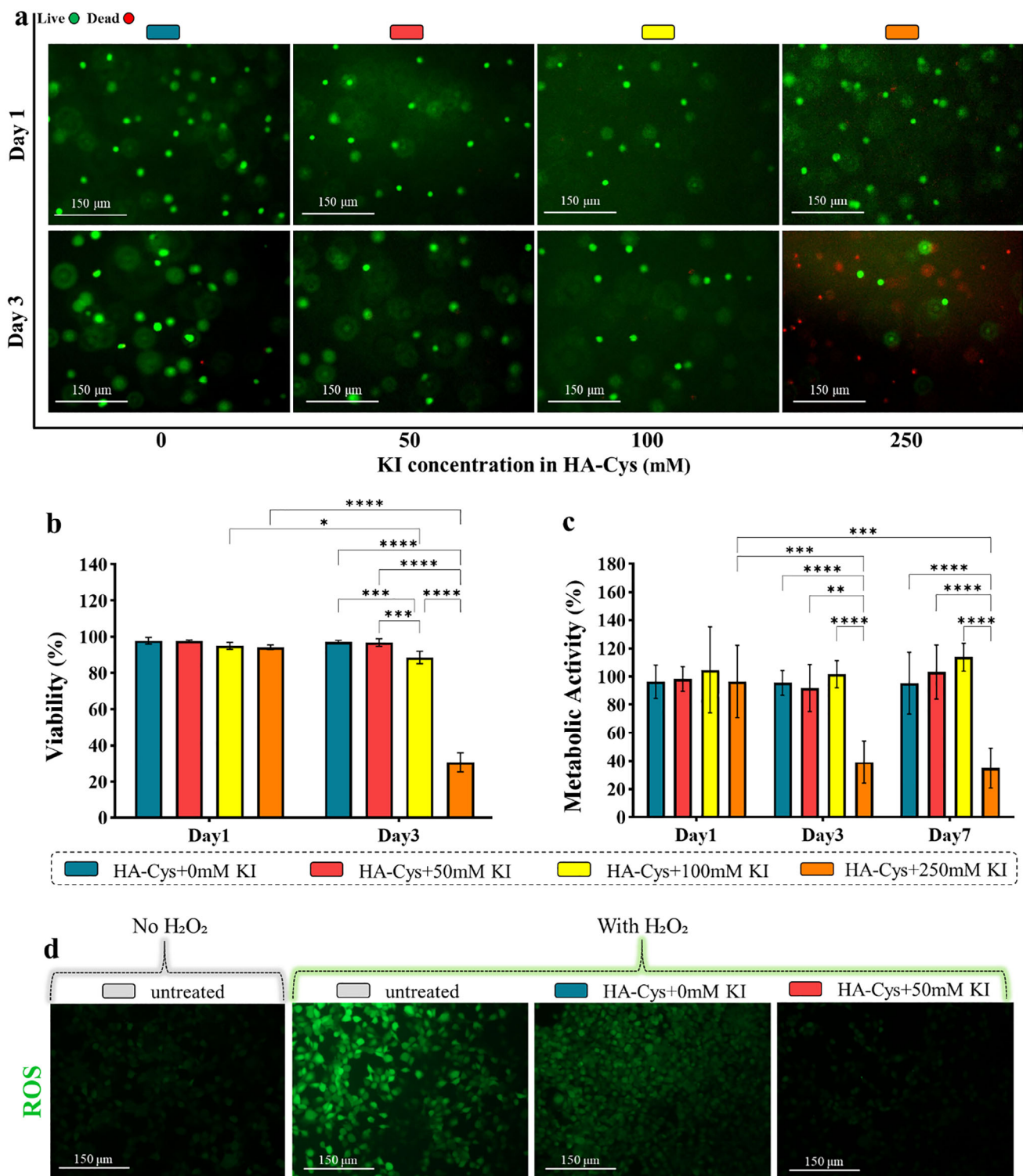


Figure 3. Effect of varying potassium iodide (KI) concentrations on the viability of encapsulated cells. a) Representative Live/Dead stained images of encapsulated chondrocyte cells at days 1 and 3 post-encapsulation. b) Cell viability percentages, calculated by comparing the number of live cells to the total number of cells using ImageJ analysis of microscopic images. c) Metabolic activity of encapsulated cells in response to different KI concentrations, assessed via the Presto Blue assay at days 1, 3, and 7. d) Fluorescent microscopic images of intracellular reactive oxygen species (ROS) visualized using dichlorodihydrofluorescein diacetate (DCFDA) staining. Statistics: Two-way ANOVA, $n = 5$ and significance is represented as: $* = p < 0.05$, $** = p < 0.01$, $*** = p < 0.001$, $**** = p < 0.0001$.

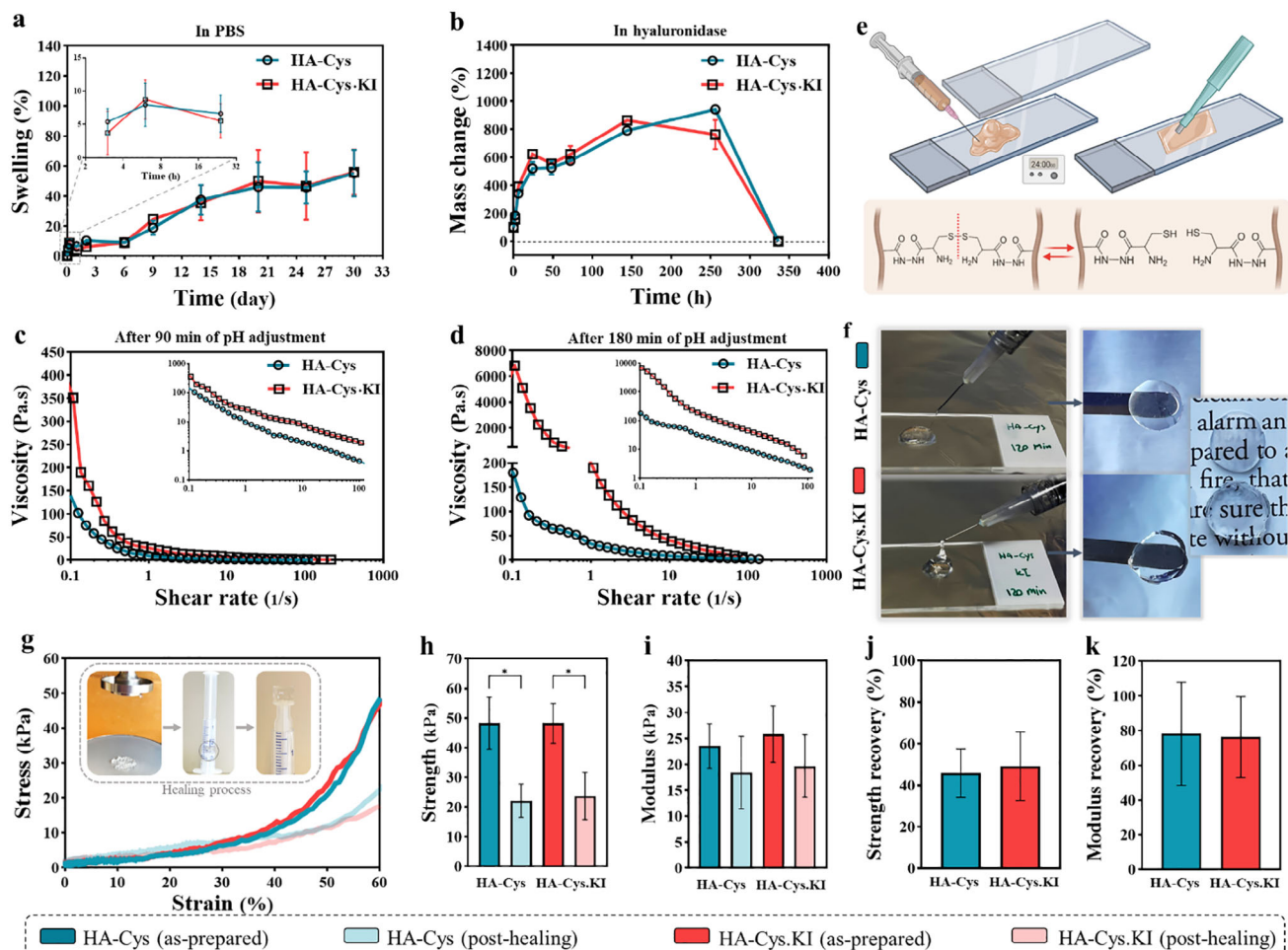


Figure 4. Effect of potassium iodide (KI) in cysteine-modified hyaluronic acid (HA-Cys) hydrogels on stability, shear-thinning, and self-healing properties. a) Swelling behavior of hydrogels in PBS at 37 °C. b) Degradation profile of hydrogels incubated in media containing hyaluronidase at 37 °C. c,d) Viscosity measurements under shear forces after 120 and 180 min of pH adjustment and crosslinking initiation (the inserts show the viscosity measurements in a logarithmic scale). e) Schematic representation of the self-healing experiment, illustrating the reformation of disulfide bonds after breaking. f) Injectability of hydrogels after 120 min of crosslinking initiation and their transparency after being fully crushed and reformed. g) Stress–strain curves comparing as-prepared and crushed-reformed (post-healing) hydrogels under up to 60% strain. h) The strength of hydrogels at 60% strain extracted from the stress–strain curve. i) The Modulus of hydrogels calculated as the slope up to 25% strain from the stress–strain curve. j,k) Recovery percentages of strength and modulus, calculated as the ratio of values post-healing to the as-prepared samples. Statistics: One-way ANOVA, $n = 3$ and significance is represented as: * = $p < 0.05$, ** = $p < 0.01$, *** = $p < 0.001$, **** = $p < 0.0001$.

treating them with H_2O_2 , thereby increasing intracellular ROS levels. Subsequently, cells were treated with HA-Cys and HA-Cys.KI, while an additional group was left untreated as a control. To assess ROS levels, we performed dichlorodihydrofluorescein diacetate (DCFDA) staining, which produces intense green fluorescence upon oxidation, allowing for visualization of intracellular ROS. In the untreated group with H_2O_2 , a strong fluorescence signal was observed, indicating high levels of ROS (Figure 3d). However, after treatment with HA-Cys and HA-Cys.KI, the fluorescence intensity decreased significantly, demonstrating a reduction in intracellular ROS. Notably, the decrease in fluorescence was more pronounced in the HA-Cys.KI group, suggesting an active role of KI in radical scavenging. These findings indicate that the HA-Cys.KI hydrogel exhibits antioxidant properties, effectively reducing intracellular ROS levels and potentially contributing to anti-inflammatory effects.

2.4. Swelling and Stability of Hydrogels in Different Conditions

Since hydrogel stability and swelling behavior are key parameters for designing a bioink, we first determined the swelling percentage of hydrogels in PBS at 37 °C over 30 days. Gratifyingly, we observed limited swelling of the two hydrogels, namely hydrogels with and without KI, with only 10% swelling during the initial 6-day period (Figure 4a). Subsequently, there was an increase in swelling for 18.8 ± 4.6% and 24.4 ± 1.1% on day 9, followed by a further increase of 37.4 ± 9.9% and 35.4 ± 11.6% by day 14, for HA-Cys and HA-Cys.KI respectively. Thereafter, the hydrogels achieved a state of equilibrium throughout the rest of the experiment time point.

The enzymatic degradability of HA hydrogels is the next parameter that we evaluated. HA is known to degrade *in vivo* in the presence of a ubiquitous enzyme hyaluronidase. Hyaluronidase

catalyzes the breakdown of β 1 \rightarrow 4 glycosidic linkages of the HA backbone.^[30] The presence of this enzyme has been seen in several organs, including the skin, eye, liver, and kidney, as well as in body fluids such as blood and tears. Additionally, to some extent, it also breaks down other mucopolysaccharides in the connective tissue.^[30] We, therefore, investigated the stability of HA-Cys hydrogels with and without KI in a hyaluronidase-rich medium at 37 °C. The weight change of the hydrogels over time was measured and expressed as a percentage of the initial weight. The hydrogel mass obtained after the initial setting (zero time point) served as the 100% reference. For this experiment, hydrogels were immersed in a hyaluronidase solution with a concentration of \approx 40 times more than the concentration of this enzyme in human plasma. As anticipated, all the hydrogels swelled noticeably in the first 6 h of incubation and continued to swell even more throughout the 10 days of the experiment (Figure 4b). Afterward, a process of deterioration ensued, resulting in the total breakdown of both hydrogels by the culmination of the experiment by day 14. The degradation profile of the two gels revealed no significant differences between the hydrogels (HA-Cys and HA-Cys.KI) in the hyaluronidase solution, suggesting that the addition of 50 mM KI to HA-Cys solution does not impact the hydrogel stability and degradation properties.

2.5. Shear-Thinning and Self-Healing Evaluation of Hydrogels

Further, the impact of disulfide crosslinking and KI on the shear-thinning properties of hydrogels was investigated. In shear-thinning materials, the viscosity of the material is expected to decrease in response to an increase in shear stress, allowing easy injection of cells through a needle, and minimizing toxicity due to the shielding effect against anoikis.^[31] Shear-thinning hydrogels, based on dynamic covalent interactions that enable reformation after the removal of shear stress, also exhibit self-healing properties. A combination of shear-thinning and self-healing behavior allows better retention of cell-loaded materials post-injection, without clogging the needle or damaging the cells, which are desirable behaviors for developing bioinks.^[32] To achieve the time points that hydrogel is suitable for 3D printing, the shear-thinning experiment was conducted 120 and 180 min after the initialization of the reaction by pH adjustment. This was achieved by gradually increasing the shear rate from 0.1 to 100 s⁻¹ and measuring the viscosity value, as observed in Figure 4c,d. After 120 min of starting the crosslinking process (pH adjustment to 7.4), the viscosity of the hydrogel composed of HA-Cys was measured to be 140 Pa s. However, the hydrogel formed by combining HA-Cys with 50 mM KI (HA-Cys.KI) exhibited a viscosity of 351 Pa s at 0.1 s⁻¹ of strain. As shown in the logarithmic scale insert of Figure 4c, the viscosity of both hydrogels decreased with increasing shear rate, dropping to 0.3 Pa s for HA-Cys and 1.2 Pa s for HA-Cys.KI, demonstrating that both hydrogels exhibit shear-thinning behavior. Additionally, the same experiment after 180 min of pH adjustment showed a similar trend, although the initial viscosity for HA-Cys and HA-Cys.KI were 149 and 6831 Pa s, respectively. The difference in the initial viscosity of hydrogels stems from the differences in gelation kinetics as a result of the addition of 50 mM KI that catalyzes disulfide formation.

Dynamic crosslinking also facilitates the self-healing properties of the hydrogel, an essential feature post-printing that helps the 3D-printed structure maintain its integrity and retain cells within the matrix.^[13] In this experiment, we explored the impact of KI on the self-healing capability of our hydrogel system. To evaluate this, we injected the hydrogels through a needle 120 min after adjusting the pH to 7.4 and adding KI (Figure 4e). Additionally, to examine the potential for broken disulfide bonds to reform, we placed the extruded gels between two glass slides and incubated them in a humidified environment at 37 °C for 24 h. As shown in Figure 4f, both hydrogels, with and without KI, fully regained their original state after injection, and demonstrated a degree of recovery. The healed hydrogels also exhibited similar transparency, indicating the re-formation of covalent disulfide bonds. We also conducted compression tests on fully crosslinked hydrogels to evaluate the strength and modulus of the gels. As shown in Figure 4g, both hydrogels, with and without KI, demonstrated similar mechanical strengths of 48.2 ± 8.7 kPa and 48.3 ± 6.6 kPa, respectively, at 60% strain. Additionally, the loading curve demonstrated that the hydrogels possess enough stiffness to withstand strains exceeding 50% of their original height without failure, highlighting their robust mechanical properties. To assess the ability of the hydrogels to recover their mechanical properties after being completely crushed, the fully smashed hydrogels were placed in isolated syringes and, after 24 h, subjected to another compression test (insert in Figure 4g). These hydrogels could heal and regain their original structures after extensive crushing, however, their strength and modulus were lower when compared to the as-prepared hydrogels (Figure 4h,i). By comparing the strength and modulus of the post-healed hydrogels to the as-prepared ones, we calculated the percentage of recovery, as presented in Figure 4j,k. These results indicate that, while the hydrogels with and without KI could not fully recover their original mechanical properties, they were able to regain more than 45% of their strength and over 75% of their modulus. These findings suggest that, although crosslinks were susceptible to disruption during extrusion and full crushing, the disulfide bonds predominantly reform, enabling partial healing of the hydrogel. Notably, the presence of KI did not interfere with this process, likely due to the dynamic nature of the disulfide bonds, which allowed disulfide exchange reactions in the presence of nearby thiolate ions.^[11]

2.6. The Impact of KI Incorporation in HA-Cys Hydrogels on Stem Cells

Cell encapsulation within a hydrogel matrix is known to affect both the mechanical behavior and degradation kinetics of the hydrogel. These changes arise from various factors, including cell-secreted metalloproteases and soluble factors in the cell culture medium, which influence the stability of the biopolymers and crosslinks and consequently, the viscoelastic properties of the hydrogel.^[33] To assess the impact of KI on the biocompatibility of the hydrogels with hMSCs, we performed Live/Dead staining on the encapsulated cells. Figure 5a presents 3D confocal microscopy images of the cells within the hydrogel, revealing uniform cell distribution throughout the matrix in both hydrogels, with a high degree of biocompatibility. To further

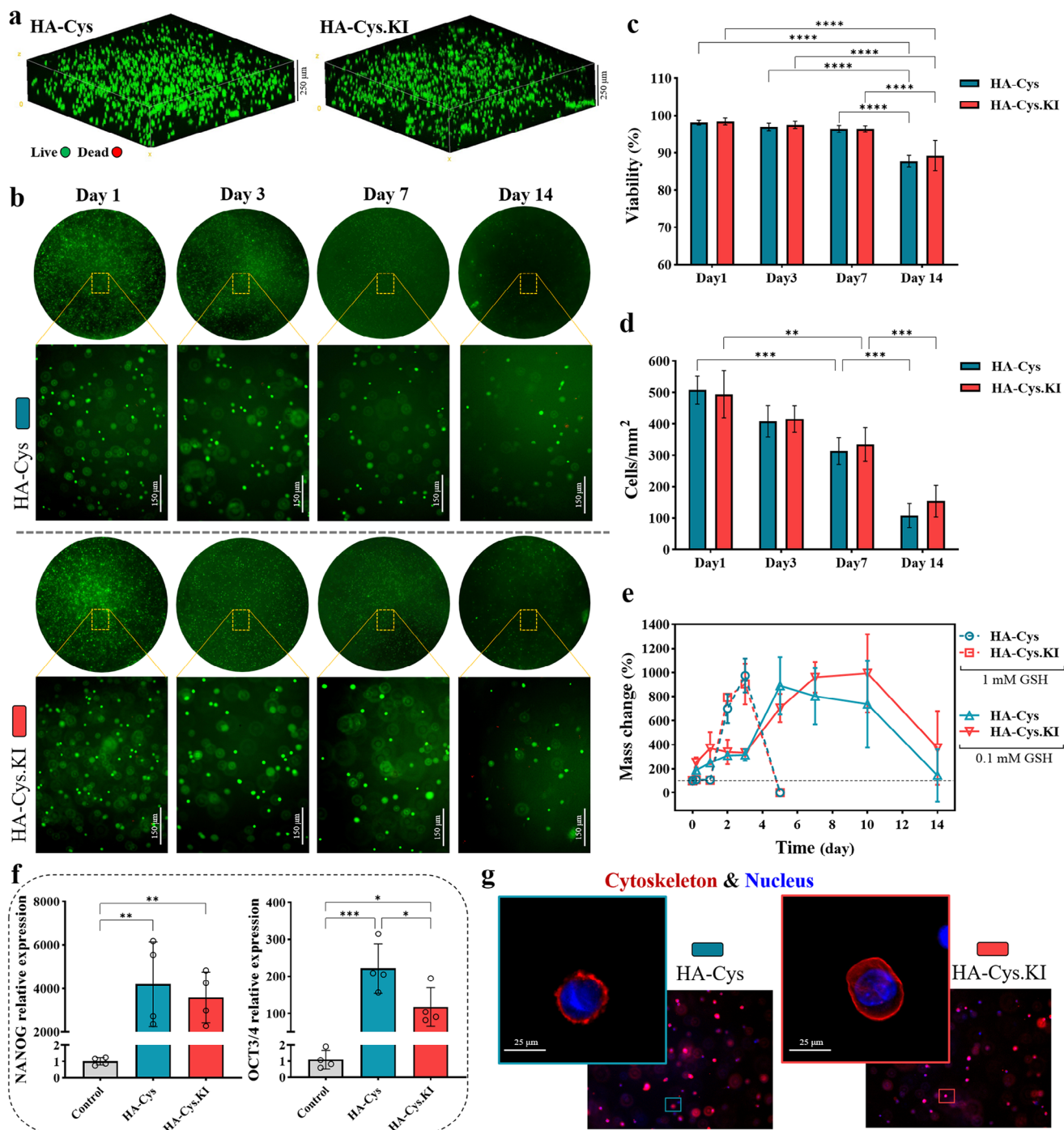


Figure 5. Impact of potassium iodide (KI) incorporation in cysteine-modified hyaluronic acid (HA-Cys) hydrogels on hMSCs behavior and hydrogel degradation. a) 3D confocal microscopy image obtained through z-stacking, showing the uniform distribution of encapsulated hMSCs within the hydrogel after 1 day. b) Fluorescence microscopy images of Live/Dead-stained hMSCs encapsulated in HA-Cys and HA-Cys.KI hydrogels over 14 days. c,d) Viability percentage and cell density of encapsulated hMSCs, analyzed from microscopy images using ImageJ software. e) Degradation profiles of HA-Cys and HA-Cys.KI hydrogels in response to glutathione (GSH) at two different concentrations. f) Relative gene expression of NANOG and OCT3/4 in encapsulated hMSCs after 5 days, as determined by qPCR. Expression levels are normalized to the control group. g) Confocal imaging of encapsulated hMSCs after 5 days, stained with phalloidin (cytoskeleton) and DAPI (nucleus) to visualize cell morphology. Statistics: Two-way ANOVA and One-way ANOVA, $n = 4-6$ and significance is represented as: * = $p < 0.05$, ** = $p < 0.01$, *** = $p < 0.001$, **** = $p < 0.0001$.

evaluate the effect of the hydrogel matrix on the encapsulated hMSCs, Live/Dead staining was conducted at 1, 3, 7, and 14 days post-encapsulation. As shown in Figure 5b, at each time point, both hydrogel formulations demonstrated a predominance of green (live) cells compared to red (dead) cells, validating the biocompatibility of the HA-Cys and KI hydrogel at a 50 mM concentration. Cell viability was also quantified by comparing the proportion of live cells to the total cell count. Both hydrogels maintained a cell viability of over 90% up to day 7, with a slight decline in viability observed after 14 days, dropping just below 90% (Figure 5c). In addition to cell viability, the cell density (cells mm⁻²) was quantified using fluorescence microscopy. As shown in Figure 5d, on day 1 post-encapsulation, the HA-Cys hydrogels, with and without KI, presented a cell distribution of 507 ± 44 and 493 ± 74 cells mm⁻², respectively. Over time, the number of cells gradually decreased, reaching ≈320 cells mm⁻² by day 7 and a reduction of more than half of the initial cell density after 14 days. This trend suggests dynamic bioactivity and interactions between the cells and the hydrogel matrix, as well as the gradual release of hMSCs from the matrix over time. This behavior is driven by the dual degradation mechanism of HA-Cys hydrogels, which are sensitive to both hyaluronidase and GSH. GSH, a tripeptide composed of glutamate, cysteine, and glycine, is synthesized within the cytosol and secreted by cells. With intracellular concentrations reaching the millimolar range, GSH is crucial for facilitating the formation of native disulfide bonds in the endoplasmic reticulum. This process is intricate, involving both the formation of new disulfide bonds and the isomerization of improperly formed, non-native bonds.^[16] When cells are encapsulated in a matrix crosslinked by disulfide linkages, the secreted GSH can interact with these bonds, reducing them and consequently altering the stability and stiffness of the hydrogels. Therefore, cell-mediated remodeling of the matrix through disulfide bond cleavage is proportional to both the cell number and their metabolic activity, enabling the gradual release of cells from the hydrogel matrix over time. To demonstrate that the stability of the hydrogel can be influenced by the concentration of GSH, a degradation experiment was conducted using two different GSH concentrations (1 and 0.1 mM). As shown in Figure 5e, both concentrations were capable of degrading the hydrogel matrix. However, at the lower concentration, it took over 14 days for the hydrogels to degrade completely, while introducing a 10 times higher amount of GSH significantly accelerated the degradation process, with the hydrogels dissolving in less than 5 days. These results corroborate our previous study which demonstrated that encapsulated hMSCs in disulfide-crosslinked hydrogels can gradually reduce the storage modulus of the gels over time.^[13]

Thus, incorporating disulfide crosslinks into HA hydrogels enables the creation of a dual-degradable matrix (GSH and hyaluronidase), facilitating controlled degradation and the release of stem cells in response to their metabolic activity and the number of encapsulated cells. Additionally, the presence of KI in HA-Cys hydrogels not only facilitates tunable degradation but also fine-tunes the gelation kinetics. Thus, the HA-Cys hydrogels are a highly versatile and adaptable platform for developing advanced bioinks or injectable living gels, with precisely controlled degradation and release mechanisms.

Further, to investigate the effect of hMSC encapsulation in HA-Cys and HA-Cys.KI hydrogels on stemness maintenance,

the expression levels of NANOG and OCT3/4 were measured using quantitative PCR (qPCR) (Figure 5f). These pivotal transcription factors are responsible for preserving pluripotency and self-renewal capacity in undifferentiated stem cells. Interestingly, compared to untreated 2D-cultured hMSCs, the expression of stemness markers significantly increased in both HA-Cys and HA-Cys.KI 3D encapsulation systems. Both NANOG and OCT3/4 exhibited a notable upregulation, suggesting that 3D encapsulation within the hydrogels plays a crucial role in maintaining or even enhancing stemness. This increase in stemness may be attributed to multiple factors. First, hypoxia-induced dedifferentiation could contribute to this effect, as oxygen availability is limited in 3D culture environments compared to 2D conditions, mimicking aspects of stem cell niches.^[34] Additionally, the interaction between HA and the CD44 receptor on hMSCs has been reported to activate the Rho/ROCK signaling pathway, which is known to support stemness and self-renewal in hMSCs.^[35] To further explore whether hydrogel-cell interactions influence cytoskeletal organization, encapsulated hMSCs were stained for F-actin (cytoskeleton) and nucleus visualization (Figure 5g). Confocal imaging revealed that cells remained round with negligible elongation in both hydrogel formulations, indicating limited cell spreading. This effect is likely due to the lack of strong adhesion moieties in the HA-based hydrogel, which prevents the formation of focal adhesions and thus restricts cytoskeletal remodeling. Notably, the addition of KI did not alter cell morphology, confirming that KI incorporation does not interfere with the structural or mechanobiological properties of the hydrogel system. The rounded morphology of hMSCs in the HA-Cys and HA-Cys.KI hydrogels could also be a contributing factor to the observed increase in stemness marker expression. Previous studies have shown that cell spreading and cytoskeletal tension influence differentiation, where elongated cells with high actin stress fiber formation are more prone to differentiation, while rounded cells experience reduced mechanical tension, which favors stemness maintenance.^[36] The restriction of cell spreading in 3D hydrogels, combined with the soft mechanical environment, likely reduces YAP/TAZ nuclear localization, further promoting a stem-like state.^[37,38] Together, these findings suggest that hMSCs encapsulation in HA-Cys and HA-Cys.KI hydrogels provide a microenvironment conducive to stemness maintenance, facilitated by hypoxia, HA-CD44 signaling, and cytoskeletal regulation. The ability of these hydrogels to preserve stem cell characteristics highlights their potential utility for in vitro modeling.

2.7. 3D Bioprinting

2.7.1. The 3D Printing Potential of HA-Cys.KI Hydrogel

One of the key ambitions of this project is to optimize the gelation kinetics with an optimal window to facilitate 3D bioprinting. We therefore probed the potential of HA-Cys.KI hydrogel as a bioink for 3D bioprinting to deliver stem cells and develop in vitro models. One of the inherent limitations of extrusion-based 3D bioprinting is its poor resolution. To address this, we first chose a needle with a gauge size of 30G, having an inner diameter of 159 μm, with pressure adjustments tailored to the hydrogel viscosity set at 250 kPa. Employing these

parameters, we printed a 3D rectangular prism model measuring 10 mm × 10 mm × 1 mm, with an infill ratio of 40%, at intervals of 60, 90, 120, 150, and 180 min post pH adjustment of the hydrogel solution. Embedded chondrocyte cells were visualized via fluorescent microscopy with Hoechst staining of the cellular nucleus. We observed a wide printing window spanning from 60 to 180 min for HA-Cys.KI hydrogel, as depicted in **Figure 6a**. Of note, this bioprinting protocol could not be optimized for HA-Cys hydrogel due to the slow gelling kinetics of such materials. To assess the print accuracy and shape fidelity of bioink, the printed structures at each time point were compared with the designed prism structure obtained from Autodesk Fusion 360 software (**Figure 6b**). Notably, at the 60-min mark, the lower viscosity of the hydrogel led to filament flow and rounded edges of the printed structures, resulting in diminished printing accuracy and shape fidelity of less than 50% compared to the original design. Extending the incubation period before printing improved the accuracy, with structures printed at the 150- and 180-min mark exhibiting enhanced precision, reaching 74 ± 7 and $86 \pm 4\%$ shape fidelity, alongside wider pores indicative of improved shape retention. Higher magnification fluorescent microscopy images of the printed filaments revealed a reduction in filament size over time, corresponding to the increase in gel viscosity (**Figure 6c**). Notably, initial time points showed a larger filament size ($\approx 400 \mu\text{m}$ at the 60-min mark), which progressively diminished to $\approx 200 \mu\text{m}$ with an increase in time (180-min time point), highlighting a significant printing window for HA-Cys.KI hydrogel as analyzed by ImageJ software (**Figure 6d**). This ensures post-printing homogeneity and uniform cell distribution within the structure. To highlight the importance of controlling gelation and optimizing the 3D printing window, we also 3D printed the same structure using HA-Cys alone at different time points following pH adjustment (**Figure S9**, Supporting Information). The results showed that after 60 min of pH adjustment, the ink failed to maintain its geometry, with a significant loss of pore structure as most pores collapsed. Although shape fidelity gradually improved over time, it remained suboptimal, and the printed structures were considerably mediocre compared to those obtained with HA-Cys.KI. This observation underscores the critical role of KI in ensuring adequate printability and structural integrity within this hydrogel system.

To further enhance the resolution of 3D printing with this hydrogel, we utilized an ultra-fine 32G needle, featuring an inner diameter of just 108 μm . As shown in **Figure 6e**, a 10 mm × 10 mm × 1 mm structure was successfully printed 180 min post pH adjustment. To the best of our knowledge, this represents the smallest size of needle utilized in 3D bioprinting with HA-based hydrogels to date. By comparing the printed structure to its original prism model and using ImageJ software, the shape fidelity was found to be $\approx 90\%$, and the filament size was measured at 115 μm (**Figure 6f**). Following this step, we utilized the same hydrogel and needle (32G) to 3D print more complex and larger structures. **Figure 6g,h** shows 3D-printed porous cube and cone structures immediately after printing. The printed structures were placed in PBS for 24 h, during which they retained their shape with high precision, closely matching the designed models. The cubic sample was subjected to compression, demonstrating the porous nature of the gels that allows it to be squeezed without breaking and subsequently return to its orig-

inal shape after the load removal (**Figure S10**, Supporting Information). Additionally, we showed that structures with larger pores could also be printed, tolerating various degrees of torsion (**Figure S11**, Supporting Information). To further explore the potential of the hydrogel to print more complex designs, we 3D printed a hollow cylinder with an outer diameter of 8 mm, a height of 20 mm, and an internal cavity of 2.5 mm in diameter. This hollow structure, which can be filled with other gels, showcases the feasibility of creating modular multi-material constructs (**Figure 6i**). This capability provides a promising platform for co-printing two different cell types within a single structure for designing advanced in vitro models. Notably, even after 24 h of swelling in PBS, the hollow structure remained intact, as shown in **Figure 6j**. Additionally, when a portion of the gel was removed from the side, the curvature of the hollow cylinder was still preserved, demonstrating its structural stability. Building on this success, we printed a more complex shape — a 50% simplified human ear. As shown in **Figure 6k** with both front and side views, the high-fidelity structures promise the potential use of such materials to create realistic in vitro tissues such as cartilage that could be used for regenerative medicine. These findings push the boundaries of 3D printing with HA-based hydrogels, enabling the fabrication of fine, highly detailed structures. This breakthrough has significant potential to revolutionize tissue engineering and regenerative medicine, offering unprecedented precision in designing biomimetic scaffolds and complex biological constructs.

2.7.2. The Effect Of Ultra-Fine 3D Printing on Chondrocytes and hMSCs

To explore the potential of our bioink to deliver sensitive human cells of different sizes and safeguard their integrity during injection through a fine needle, we injected cells through a 32G needle. Previous studies have suggested that cells exposed to syringe needle flow are subjected to mechanical shear and extensional forces, which can compromise the cell membrane. This effect is more pronounced when cells are injected in low-viscosity solutions such as saline or cell culture medium.^[39–41] For this experiment, we selected hMSCs and human chondrocytes because hMSCs are larger ($\approx 20\text{--}50 \mu\text{m}$) while chondrocytes represent cells with smaller sizes ($\approx 10\text{--}20 \mu\text{m}$). In this case, hMSCs and chondrocyte cells were stained for visualization and encapsulated in HA-Cys hydrogel containing 50 mM KI. As shown in **Figure 7a**, both hMSCs and chondrocytes were successfully printed by a 32G needle, either separately or side-by-side in different filaments. The cells were evenly distributed within the printed filaments, demonstrating homogenous encapsulation and printability of the cell-laden hydrogel. To evaluate the efficacy of the hydrogel in promoting cell survival after extrusion, a cell culture medium was used as a comparative carrier for the cells. The cells were separately injected using a 3D bioprinter with a 32G needle and identical pressure conditions. To assess plasma membrane damage during injection, the release of LDH was quantified using a colorimetric assay. The LDH release experiment showed differences in cell viability as a result of compromised cell membrane integrity between hMSCs and chondrocytes across both groups (**Figure 7b**). Overall, hMSCs exhibited lower

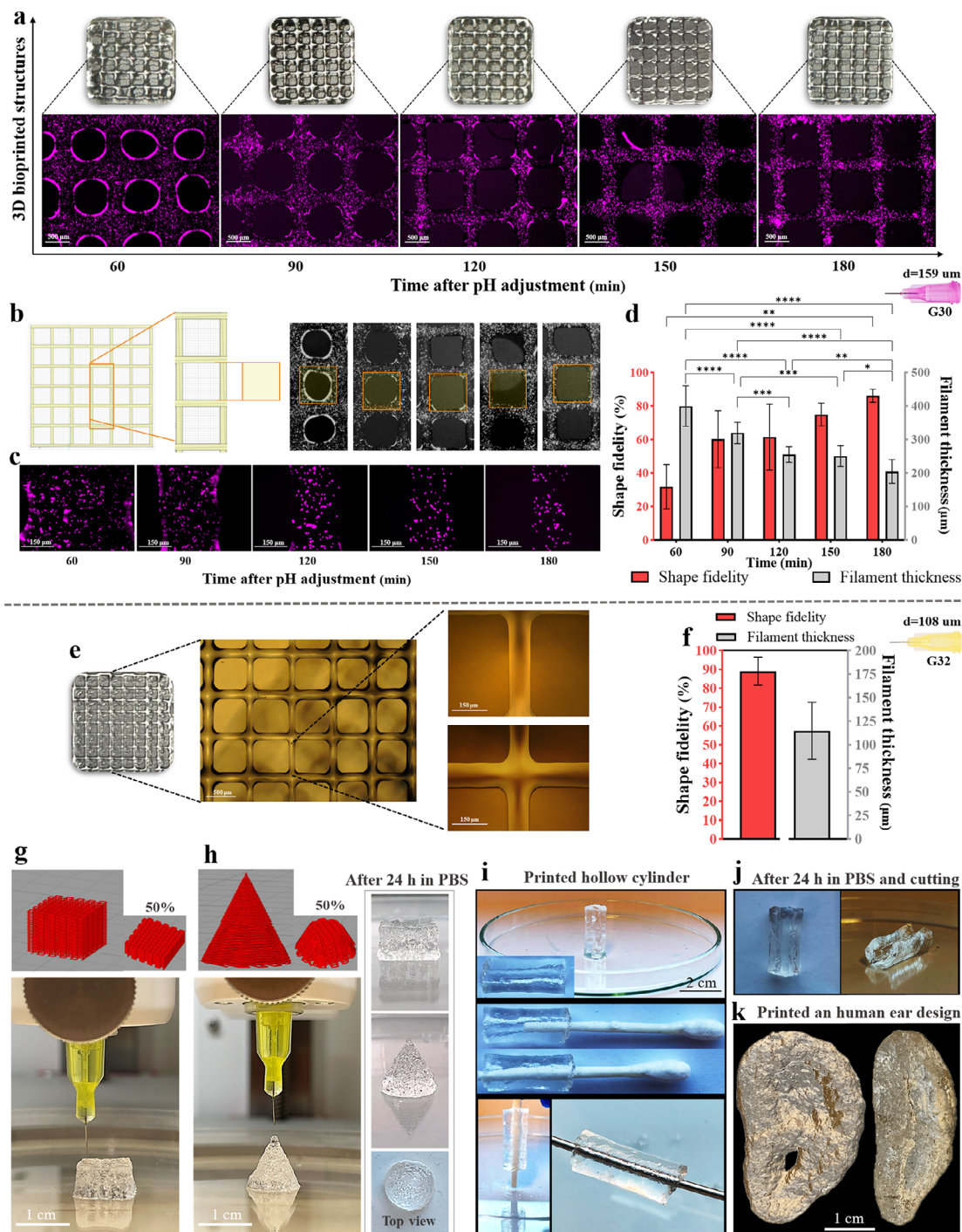


Figure 6. Optimization of 3D bioprinting with potassium iodide (KI) incorporated cysteine-modified hyaluronic acid (HA-Cys.KI) hydrogel. a) Digital and fluorescence microscopy images of HA-Cys.KI hydrogel loaded with chondrocyte cells, printed using a 30G needle, at different time points post pH adjustment. b) Comparison of the designed print structure with printed samples at various time points, with shape fidelity analyzed using ImageJ software. c) Higher-magnification fluorescence microscopy images of filaments printed with a 30G needle, highlighting structural details at different pH adjustment intervals. d) Quantitative analysis of shape fidelity and filament thickness of HA-Cys.KI hydrogel printed with a 30G needle at various pH adjustment times. e) Digital and microscopy images of HA-Cys.KI hydrogel, printed using a 32G needle after 180 min of pH adjustment. f) Quantitative analysis of shape fidelity and filament thickness for hydrogel printed with a 32G needle after 180 min of pH adjustment. g,h) 3D-printed cube and cone structures using HA-Cys.KI hydrogel, shown immediately after printing and following 24 h of swelling in PBS. i) 3D-printed hollow cylinder, with its cavity visually demonstrated by filling with a Q-tip and a metal rod. j) Digital images of the hollow cylinder after cutting a portion of the structure, showing preservation of curvature. k) Digital images of a 50% simplified 3D-printed human ear, displayed from front and side views. Statistics: Two-way ANOVA, $n = 7$ and significance is represented as: * = $p < 0.05$, ** = $p < 0.01$, *** = $p < 0.001$, **** = $p < 0.0001$.

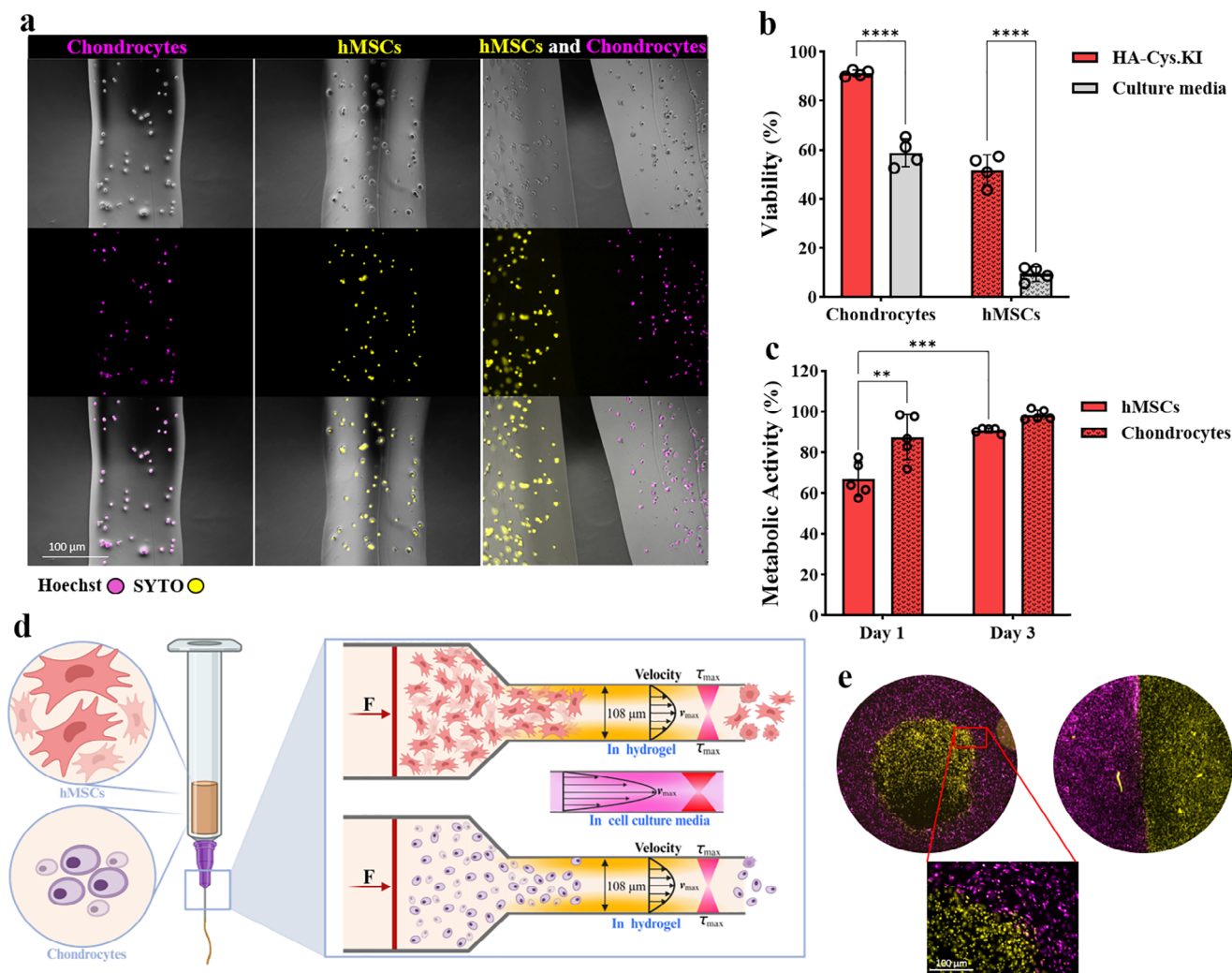


Figure 7. 3D bioprinting with two different cell types and the impact of printing on cell viability. a) Fluorescence microscopy images of 3D-printed filaments of potassium iodide (KI) incorporated cysteine modified hyaluronic acid (HA-Cys.KI) hydrogel loaded with chondrocytes and hMSCs, printed either separately or combined within the same structure. b) Comparison of cell viability percentages between cells printed with HA-Cys.KI and cells extruded directly with culture media through a 32G needle under the same pressure. c) Metabolic activity of chondrocytes and hMSCs 1 and 3 days post-printing via a 32G needle. d) Schematic representation of the 3D bioprinting process using HA-Cys.KI hydrogels, highlighting the effects of shear forces on chondrocytes and hMSCs during printing. It also demonstrates the differences in shear forces when injecting cells through cell culture media and hydrogel. e) Fluorescence microscopy image of a 3D-printed disc of HA-Cys.KI hydrogel loaded with chondrocytes, filled with HA-Cys.KI hydrogel containing hMSCs, and a structure where both cell types were printed directly adjacent to one another. Statistics: Two-way ANOVA, $n = 4-5$ and significance is represented as: * = $p < 0.05$, ** = $p < 0.01$, *** = $p < 0.001$, **** = $p < 0.0001$.

viability compared to chondrocytes, regardless of whether the injection was performed with the hydrogel or cell culture medium. This is likely due to the larger size of hMSCs, making them more prone to membrane damage and LDH release during injection. However, as shown in Figure 7b, the hydrogel demonstrated a greater ability to protect both cell types from shear forces during extrusion as compared to the cell culture medium. Specifically, over 90% of chondrocytes survived when injected with the hydrogel, while only $\approx 50\%$ of cells survived when injected with cell culture media. This trend was even more pronounced with hMSCs, where $52 \pm 6\%$ of cells survived injection when delivered using hydrogel, while only $9 \pm 3\%$ of stem cells survived when delivered using cell culture media. These findings under-

score the superior capacity of the hydrogel to protect cells from shear-induced damage and anoikis during 3D printing. This result agrees with our previous observation that injecting stem cells through a stable HA-based bioink impacts cell survival as compared to cell culture media.^[13]

We also assessed the relative metabolic activity of the printed cells at 1 and 3 days post-printing using the Presto Blue assay (Figure 7c). This experiment revealed that the cells that survived the shear forces were metabolically active and proliferated over time. Specifically, chondrocytes exhibited an increase in metabolic activity from $87 \pm 11\%$ on day 1 to $98 \pm 3\%$ by day 3, while hMSCs increased from $67 \pm 8\%$ to $91 \pm 2\%$ over the same period. These findings indicate that, although 3D bioprinting

may cause initial damage to hMSCs, the hydrogel matrix mitigated the cellular shear stress and helped cell recovery and maintain metabolic activity following printing. It is expected that the cells experience different shear forces as they pass through the needle, with the highest stress occurring on cells in contact with the needle walls (Figure 7d). This effect is more profound in low-viscosity media as compared to the hydrogel. Such forces lead to membrane damage, anoikis, and apoptosis, an issue particularly relevant for hMSCs, which are more vulnerable to shear stress due to their larger size compared to chondrocytes. This prompted us to design two different bioprinted patterns where hMSCs (labeled with SYTO) were printed in the middle of a cylindrical design and chondrocytes (labeled with Hoechst) in the periphery as well as another cylindrical design where the two-cell types were printed side-by-side (Figure 7e). This successful bioprinting of two different cell types in distinct patterns encouraged us to create more complex in vitro 3D models to study cell–cell and cell–material interactions.

2.8. 3D Bioprinting of In Vitro Tissue and Disease Models

3D printed tissue models with high shape fidelity and precise cell distribution enable the development of complex and biologically relevant in vitro models, offering a platform to study cellular interactions within a 3D environment.^[42] We therefore investigated the migration of hMSCs and chondrocytes in a 3D-printed in vitro model. For this, hollow cylinders—either cell-free or cell-laden—were fabricated directly in a well plate. Subsequently, the hollow inner region of these cylinders was filled with either cell-free or cell-laden hydrogel (Figure 8a). To design 3D models with different cell distribution, we considered three different scenarios: 1) Model 1: A hollow cylindrical gel encapsulated was printed and subsequently, the center cavity was filled with cell-free gel; 2) Model 2: A cell-free hollow cylinder was printed first and the center cavity filled with hMSCs-laden bioink; and 3) Model 3: A multicellular construct was printed where the hollow cylinder was printed with chondrocytes while the center cavity was filled with hMSCs-laden bioink. In these 3D models, we employed a similar cell density of hMSCs and chondrocytes within the bioink, however, the volume needed to create the model required different bioink volumes for the hollow cylinder and the cavity. To visualize cell migration over time the hMSCs and chondrocytes were labeled with DiL and DiO (Vybrant cell-labeling solutions), respectively. The green fluorescent color represents chondrocytes while the red cells represent hMSCs. The 3D-printed scaffold was cultured over 7 days and the real-time cell migration was monitored at different time points using a fluorescent microscope. As illustrated in Figure 8b there were no significant structural changes or cellular movement after 1 day of encapsulation. However, by day 2 in model 1, the chondrocytes began migrating toward the center and filled the cell-free area in the middle after day 3. In contrast, hMSCs in model 2 displayed delayed migration, which was initiated around day 7. In the case of model 3, we observed a unidirectional migration of hMSCs toward the chondrocytes at day 5, while the chondrocytes exhibited limited migration toward the hMSCs. The migration distance at different time points was quantified using ImageJ software (Figure 8c). This behavior highlights the importance of paracrine signaling in mediating cell–

cell communication and migration between MSCs and chondrocytes, closely resembling in vivo conditions. In the absence of hMSCs, chondrocytes exhibited enhanced migratory properties. However, when hMSCs were present in close proximity, chondrocyte migration was reduced, while hMSCs showed increased migration toward chondrocytes. This phenomenon reflects clinical scenarios where transplanted hMSCs migrate toward chondrocytes in the synovium of osteoarthritis patients, driven by chondrogenic factors, thereby stimulating tissue repair and promoting healing.^[43]

Finally, we developed a 3D-printed osteoarthritis inflammation disease model using inflammation-induced chondrocyte cells. Four experimental groups were designed for this study (Figure 8d). Hollow cylindrical hydrogels composed of HA-Cys were fabricated using a 3D printer, with the inner hollow spaces filled with HA-Cys hydrogels containing different cell types. 1) Control: Hollow cylinders filled with hydrogels containing chondrocytes to serve as a baseline; 2) #Control: Cylinder filled with hydrogels encapsulating inflammation-induced chondrocytes to model osteoarthritis conditions; 3) #KI: The cavity filled with inflammation-induced chondrocytes encapsulated in HA-Cys.KI to evaluate the effect of KI on inflammation markers; 4) #Co-culture: hMSCs were encapsulated in HA-Cys within the hollow cylinder, while the cavity was filled with hydrogels containing inflammation-induced chondrocytes, to explore the interaction between hMSCs and inflammatory chondrocytes. As it is shown in Figure 8e, we analyzed the expression levels of major pro-inflammatory genes, including TNF- α and IL-1 β . As expected, stimulated chondrocytes exhibited significantly elevated mRNA expression of both TNF- α and IL-1 β compared to the control group. Interestingly, in the group where stimulated chondrocytes were encapsulated in HA-Cys.KI hydrogel, the mRNA expression levels of IL-1 β and TNF- α were notably reduced. This reduction underscores the anti-inflammatory potential of KI, likely due to its potent radical scavenging ability. By neutralizing ROS generated during inflammatory responses, KI can diminish the activation of nuclear factor-kappa B (NF- κ B), a key regulator of pro-inflammatory cytokine production, thereby reducing the downstream expression of TNF- α and IL-1 β .^[44] When hMSCs were present in the surrounding environment of inflammatory chondrocytes, a more complex interaction was observed. The level of TNF- α mRNA expression increased, whereas IL-1 β levels decreased significantly. The enhanced TNF- α expression may reflect a pro-inflammatory response mediated by hMSC paracrine signaling under specific conditions, as hMSCs are known to modulate immune responses bidirectionally based on environmental cues. Conversely, the marked reduction in IL-1 β suggests that hMSCs may exert anti-inflammatory effects by secreting factors such as prostaglandin E2 (PGE2) or TGF- β , both of which are known to suppress IL-1 β expression.^[45,46] Further analysis of IL-6, TGF- β , and IL-10 mRNA expression levels revealed distinct effects of KI and hMSCs. While the presence of KI (#KI group) did not affect IL-6 levels, it significantly increased TGF- β expression, and a milder increase was also observed in IL-10 expression, likely reflecting a shift toward a regenerative phenotype supported by the antioxidant environment. In contrast, the presence of hMSCs (#hMSCs group) led to a significant increase in both IL-6 and TGF- β expression and a slight increase in IL-10 level. This upregulation suggests that hMSCs not only

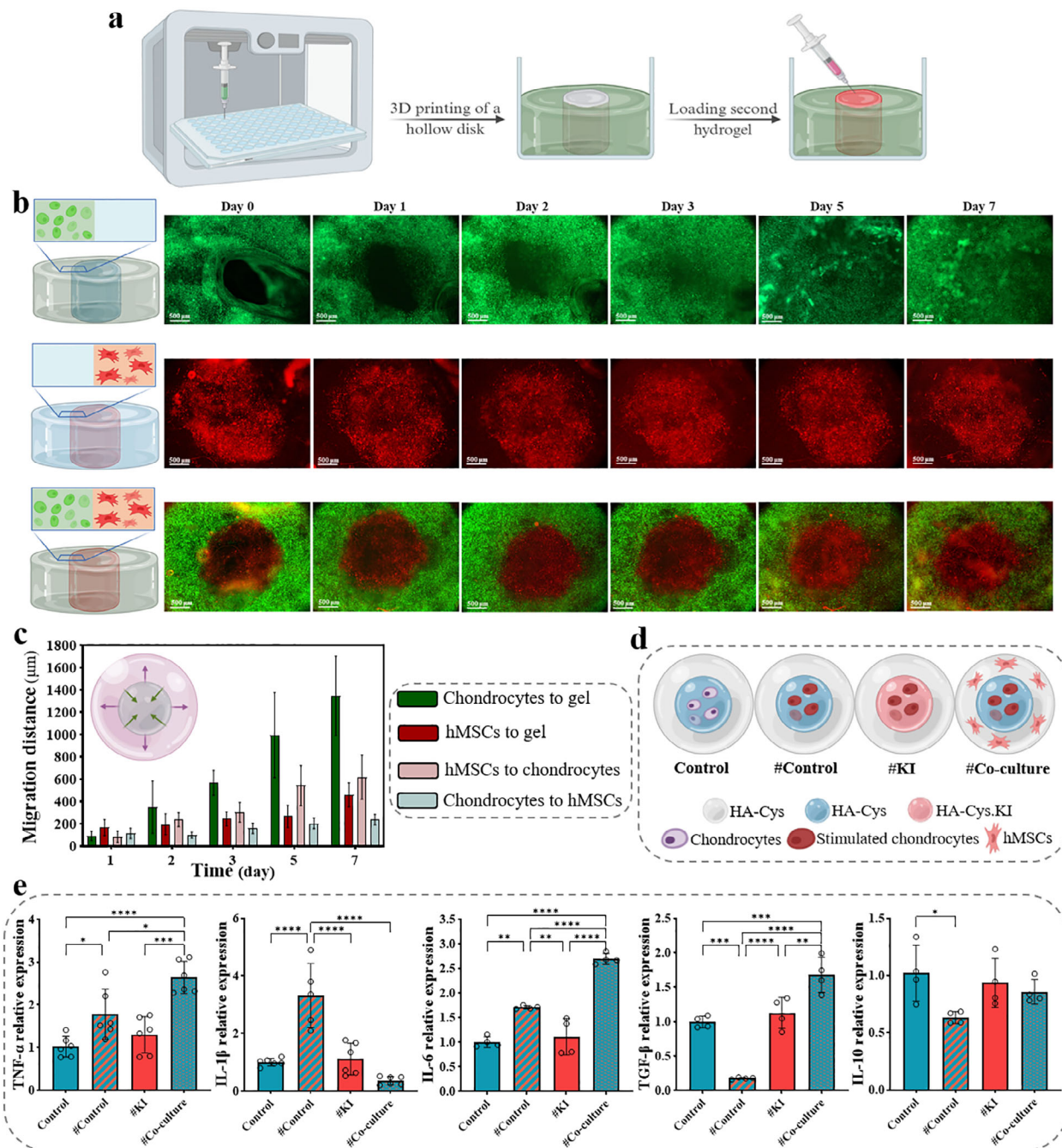


Figure 8. 3D bioprinting of in vitro models. a) Schematic illustration of the 3D bioprinting process to create in vitro models for studying the migration of hMSCs and chondrocytes. b) Fluorescent microscopy images showing real-time cell movement within the hollow cylinder with infill printed structures over 7 days. c) Quantified migration distance of cells at different time points in the hollow cylinder with infill structures. d) Schematic representation of the experimental groups used in the osteoarthritis in vitro model groups. # represents inflammation-induced chondrocytes. Statistics: Two-way ANOVA and One-way ANOVA, $n = 4-6$ and significance is represented as: * = $p < 0.05$, ** = $p < 0.01$, *** = $p < 0.001$, **** = $p < 0.0001$.

enhance inflammatory signaling via IL-6 but also promote tissue repair and matrix remodeling through elevated TGF-β and IL-10 levels, emphasizing the dual role of hMSCs in both inflammation and repair. Additionally, we demonstrated that the combination of KI and hMSCs (#Co-culture.KI group) significantly modulates inflammatory and pro-inflammatory mark-

ers (Figure S12, Supporting Information). Interestingly, this effect closely reflected that of the #Co-culture group without KI, suggesting that hMSCs exert a more dominant influence than KI alone. This dynamic highlights the complex interplay between KI, hMSCs, and cytokine signaling, emphasizing the utility of this model for investigating therapeutic strategies targeting

inflammation and tissue degeneration in conditions such as osteoarthritis.

3. Conclusion

In this study, we have developed a novel ECM-mimetic bioink tailored for 3D bioprinting. By leveraging a single-component system derived from cysteine-modified HA and optimizing gelation kinetics with KI as a catalyst, we achieved significant advancements in bioink performance. This disulfide-crosslinked hydrogel demonstrated exceptional properties, including precise gelation kinetics, shear-thinning behavior, and the ability to maintain shape fidelity after printing. This result also underscores the importance of optimizing gelation kinetics and crosslinking mechanisms to create bioinks to 3D print complex models with ultra-fine needles. The dual-degradability of this hydrogel, modulated by the type and density of encapsulated cells, further enhances its versatility. Notably, our one-component system potentially enables the encapsulation of multiple cell types, such as stem cells, cancer cells, and immune cells, in customizable designs. This functionality facilitates the study of complex cellular interactions and crosstalk, unlocking new possibilities for disease modeling and tissue engineering. To demonstrate the unique properties of our hydrogel, we 3D bioprinted an osteoarthritis disease model *in vitro*, where the immunomodulatory effect of hMSCs on inflammation-induced chondrocytes was studied in a 3D-controlled environment. Our biomaterial design strategy marks a significant step toward the development of ECM-mimetic bioinks for 3D bioprinting. This strategy is broadly applicable, as cysteine functionalization can be used to modify various biopolymers, thereby extending this crosslinking approach to a wide range of bioink materials. However, the practical incorporation of cysteine may be limited, as it requires the presence of carboxylate groups on the polymer backbone. Furthermore, thiol oxidation presents an additional challenge, as cysteine-functionalized building blocks may require storage under inert conditions to maintain stability. By optimizing the dynamic crosslinking kinetics, we have achieved a balance of properties that positions this bioink as a transformative tool for constructing advanced *in vitro* models. These advancements pave the way for the next generation of bioinks, tailored to address the most demanding challenges in disease modeling, precision medicine, and therapeutic innovation. Ultimately, our findings offer immense potential to elevate standards in healthcare and regenerative medicine.

4. Experimental Section

Materials: HA (MW 200 kDa) was purchased from LifeCore Biomedical (Chaska, USA). Other chemicals including 1-ethyl-3-(3-dimethylaminopropyl)-carbodiimide hydrochloride (EDC), 1-hydroxy benzotriazole hydrate (HOBt), 3- amino 1,2- propanediol, dithiothreitol (DTT), and potassium iodide (KI), were purchased from Sigma-Aldrich. Dialysis membranes used for purification were purchased from Spectra Por (Spectra Por-3, MWCO 12–14 kDa).

Synthesis of Cysteine-Modified HA and Hydrogel Formation: To modify HA with cysteine groups, the previously reported procedure was adapted as described below.^[20] Briefly, 0.4 g of HA (1 mmol, 1 eq with respect to disaccharides) and HOBt (0.135 g, 1 mmol, 1 eq) were dissolved in 50 mL of deionized water. To this solution, 0.310 g of 3,3'-dithiodi(2-aminopropanehydrazide) (0.9 mmol, 0.9 eq) was added and stirred until

a clear solution was obtained. The pH of the solution was adjusted to 4.7 using 1 M NaOH or HCl. Next, 0.042 g of EDC (0.22 mmol, 0.22 eq) was added in two portions while maintaining the pH at 4.7. The reaction mixture was stirred at room temperature overnight. Thereafter, DTT (0.771 g, 5 mmol, 5 eq) was added, and the reaction mixture was stirred overnight at room temperature. The mixture was then diluted to a concentration of 4 mg mL⁻¹, and the pH was adjusted to 4.5 by adding 1 M HCl. The mixture was then dialyzed against a dilute HCl solution (pH 5) containing NaCl (0.1 M) under nitrogen gas purging for 24 h, with two changes of dialyzing solvent. This was followed by dialysis against dilute HCl (pH 5) with nitrogen gas purging for an additional 24 h, again with two changes of dialyzing solvent. The obtained solution was then lyophilized to obtain the cysteine-modified HA (HA-Cys). The conjugation of thiol functionality was confirmed through ¹H NMR analysis, which can be found in the supporting information. The modification percentage was also assessed using Ellman's test, employing DTNB reagent. The concentration of free thiols in HA-Cys was determined by measuring the absorption at 412 nm using a UV-vis spectrometer and comparing with a standard curve.

In order to prepare the hydrogels, the synthesized HA-Cys was initially dissolved in a degassed PBS at pH 5.0 to obtain a homogeneous 2% solution, which was then adjusted to pH 7.4 using 2 M NaOH to initiate the gelation. Additionally, to prepare the hydrogels with faster gelation kinetics, different volumes of KI solution (1 M) were added prior to pH adjustment to obtain HA-Cys hydrogels containing 10, 25, 50, 100, 250, and 500 mM KI with the final solid content of the hydrogels set to 2%. Before conducting experiments involving cell encapsulation, the hydrogel materials underwent rigorous UV sterilization for 20 min and were subsequently dissolved under sterile conditions.

Rheological and Mechanical Characterization: To assess the rheological properties of the hydrogels, 200 μ L volumes of each group were prepared in the form of cylinders with a diameter of 8 mm and left to cure for 24 h in a humid environment at room temperature. The TA instruments, TRIOS Discovery HR 2 rheometer was then used to evaluate the storage modulus (G') and loss modulus (G'') values through an amplitude-sweep, which was then plotted against the strain to demonstrate the viscoelastic shear behavior of the hydrogels. Additionally, the G' values for each sample at 1% strain were reported to compare different groups.

Gelation time was also determined using the same rheometer, with all measurements conducted inside a humidity chamber to prevent hydrogel desiccation. After pH adjustment, the solutions of the HA derivatives (450 μ L) were immediately transferred to the rheometer, and the gap was adjusted to a size of 500 μ m. Using 20 mm parallel plate geometry (strain, 1%; frequency, 0.5 Hz), the storage and loss modulus were recorded over time, and the gelation time was defined as the point at which G' crossed G'' . Furthermore, the shear-thinning and injectability behavior of the hydrogels were also monitored by measuring the viscosity (η^*) against different shear strains after 120 and 180 min of KI addition and pH adjustment to 7.4.

To evaluate the self-healing properties of the hydrogel after injection, the following procedures were employed. After a pH adjustment, hydrogels were allowed to crosslink for 120 min before extrusion through a needle. The extruded hydrogels were then placed between glass slides with some spacing and left undisturbed overnight at 37 °C. Following this period, the formed gel was punctured using an 8 mm biopsy punch, and the transparency of the gel was assessed visually. For a more detailed evaluation of the self-healing capabilities of hydrogels, 400 μ L of the hydrogel was loaded into an 8 mm diameter syringe mold and allowed to cure overnight. These samples were subjected to a compression test to establish the baseline mechanical properties, referred to as "prepared gels." After complete mechanical crushing, the gels were reloaded into the mold, compressed using a syringe piston, and left again overnight to allow recovery. The recovered gels were again subjected to compression testing. Stress-strain curves were plotted for both "as prepared" and "post-healing" samples, and the compressive strength at 60% strain, as well as Young's modulus up to 25% strain, were calculated. The percentage recovery for both the compressive strength and modulus of the gels was determined by comparing the values obtained from the after-healing gels to those of the initially prepared gels.

Swelling and Degradation of Hydrogels: To study the degradation and swelling characteristics of the hydrogels, prepared samples were subjected to different conditions including PBS pH 7.4, hyaluronidase (250 U mL⁻¹) solution, and glutathione (GSH) solution (0.1 and 1 mM) in PBS at 37 °C. Briefly, 250 µL gels were prepared in an 8 mm mold and kept for 24 h to complete the gelation, and then placed in a glass vial, the initial weight of the hydrogels was also recorded. The gels were then submerged in PBS with pH 7.4 for swelling study. To determine hydrogel degradation hyaluronidase and GSH solution were employed in PBS. To observe the swelling and subsequent stability characteristics of the hydrogels, at different time points, the solution was taken out and gels were weighed, afterward, the buffer solution was replaced with a fresh solution. The remaining weight percentage was calculated by using the Equation (1). Additionally, Equation (2) was employed to calculate the swelling percentage for the samples.

$$\text{Mass change (\%)} = \frac{\text{Measured weight}}{\text{Initial weight}} \quad (1)$$

$$\text{Swelling (\%)} = \frac{\text{Measured weight} - \text{Initial weight}}{\text{Initial weight}} \quad (2)$$

Radical Scavenging Evaluation: The DPPH (2,2,1-diphenyl-1-picrylhydrazyl) reagent was used to investigate the free radical scavenging activity of HA-Cys with different concentrations of KI (0, 25, 50, 100, and 250 mM). A solution of DPPH was made by dissolving 8 mg of DPPH in 50 mL of absolute ethanol. The absorbance of the DPPH solution was adjusted to ≈1.1 at 517 nm using a microplate reader to maintain the desired initial concentration. The crosslinked hydrogels were afterward substituted inside the 24-well plate, followed by the addition of 300 µL of DPPH solutions, followed by 30 min incubation at room temperature. Thereafter, the absorbance was determined at 517 nm, and the DPPH scavenging activity was calculated using Equation (3).

$$\text{The scavenging activity (\%)} = \left[\frac{(A_0 - A_{\text{sample}})}{A_0} \right] \times 100 \quad (3)$$

A_0 represents the absorbance of the blank DPPH solution, and A_{sample} denotes the absorbance of the solution in the presence of polymer samples.

Cell Culture: The C2812 (human chondrocyte cells) were cultured in T-75 cell culture flasks using Dulbecco's Modified Eagle Medium/Nutrient Mixture F-12 with GlutaMAXTM (DMEM/F12, GlutaMAXTM). The medium was supplemented with 10% fetal bovine serum (FBS) (Gibco) and 1% Antibiotic-Antimycotic (AA), and the cells were maintained in a cell culture incubator at 37 °C with a CO₂ concentration of 5%. Medium replacement occurred every two days, and cells were passaged upon reaching ≈80% confluency. The stem cells namely, hMSCs were cultured in T-150 cell culture flasks using Dulbecco's Modified Eagle Medium (DMEM, Gibco) supplemented with 10% FBS (Gibco) and 1% AA under similar conditions. Cells from passages 2–6 were utilized for the experiments.

Prior to encapsulation, cells were detached from the flasks using TrypLE Select (Gibco), followed by centrifugation and resuspension in a complete medium. After cell counting, the required number of cells was centrifuged again, and the resulting pellets were resuspended in a pH-adjusted HA-Cys solution to 7.4 followed by the addition of KI solutions. The freeze-dried HA-Cys were sterilized under UV light for 20 min before dissolution in the buffer.

Biocompatibility and Live/Dead Staining of 3D Encapsulated Cells: To investigate the impact of varying concentrations of KI on chondrocyte cells, cell encapsulation was conducted within HA-Cys hydrogels using KI concentrations of 0, 50, 100, and 250 mM. The pH of the HA-Cys solution was adjusted to 7.4 for each group, and KI concentrations were introduced into the polymer solutions accordingly. C2812 chondrocyte cells were encapsulated at a concentration of 0.5×10^6 cells mL⁻¹ in the hydrogels, with each sample placed into a 96-well plate at a final volume of 100 µL. After 1 h incubation for gelation, 200 µL of media was added to each sample, and the

plate was placed in a cell culture incubator. Media was replaced every two days.

To assess cell viability over time, Live/Dead staining (Viability/Cytotoxicity Kit for mammalian cells, ThermoFisher) was performed after 1 and 3 days of incubation. Hydrogels were washed with PBS and then incubated with 200 µL of Live/Dead staining solution (containing 2 µL mL⁻¹ Calcein AM and 4 µL mL⁻¹ Ethidium homodimer in cell culture medium) for 1.5 h at 37 °C. After incubation, hydrogels were washed again with PBS and imaged using a Nikon Eclipse Ts 2 fluorescence microscope with 2× and 10× objectives. Image analysis was conducted using ImageJ software, with cell viability determined by comparing the number of green cells (live) to the total number of green and red cells (dead).

Additionally, the Presto Blue assay, a resazurin-based reagent, was employed to assess cell viability and cytotoxicity. After incubating the hydrogels for 0, 1, 3, and 7 days, they were washed with PBS, and a 220 µL volume of a 5% Presto Blue solution (ThermoFisher) was added to each gel. The mixture was incubated for 6 h, after which fluorescence intensity was measured using a plate reader set to an excitation of 560 nm and an emission of 590 nm.

Furthermore, hMSCs were encapsulated in HA-Cys hydrogels formulated with either 0 or 50 mM KI (optimal concentration). The cell density was considered at 1×10^6 cells mL⁻¹ for both groups. Live/Dead staining was conducted on these samples after incubation for 1, 3, 7, and 14 days. To assess cell distribution on day 1, z-stack 3D images were acquired using a confocal microscope, providing a detailed visualization of the encapsulated cells in 3D. At subsequent time points, imaging was performed using a fluorescence microscope equipped with 2× and 10× objectives to monitor cell viability and cell number using ImageJ software over time.

Intracellular ROS Staining: To evaluate the impact of HA-Cys and HA-Cys with 50 mM KI hydrogels on cell response under oxidative stress, a DCFDA fluorescence staining assay was performed. For the staining, 15 000 cells per well were seeded into a 48-well plate and incubated overnight to allow cell attachment. The next day, cells were further incubated with 400 µM H₂O₂ for 24 h to induce oxidative stress. Following this, HA-Cys and HA-Cys + 50 mM KI hydrogel solutions were prepared at a concentration of 1 mg mL⁻¹ in culture media. These solutions were added to the cell culture medium, while a separate control group without H₂O₂ treatment was included as a negative control. The media on top of the cells was replaced with the hydrogel-containing medium, and the plate was incubated for 24 h. After incubation, the medium was aspirated, and the cells were washed twice with PBS. The cells were then incubated in a 10 µM solution of DCFH-DA for 30 min and kept in the dark at 37 °C. DCFH-DA was a cell-permeable, non-fluorescent dye that, in the presence of reactive oxygen species (ROS) such as H₂O₂, was oxidized to form dichlorofluorescein (DCF), a highly fluorescent molecule. After staining, the DCFDA solution was removed, and the cells were washed twice with PBS. Finally, fluorescent images were captured using a fluorescence microscope equipped with a 10× objective to assess intracellular ROS levels.

Stemness of Encapsulated hMSCs: To investigate the effects of HA-Cys and HA-Cys.KI hydrogels on the stemness of hMSCs, 2×10^6 hMSCs mL⁻¹ (passage number 2) were encapsulated within the hydrogels. The encapsulated cells were then covered with cell culture media and incubated at 37 °C for 5 days. Following the incubation period, the hydrogels were enzymatically degraded by treating them with 1000 U mL⁻¹ hyaluronidase for 2 h, followed by mechanical crushing to fully dissolve the matrix. The resulting cell suspension was collected by centrifugation, lysed using lysis buffer, and RNA extraction was performed using the RNeasy Plus Mini Kit (Qiagen) following the manufacturer's protocol. Subsequently, cDNA synthesis was carried out, and the samples were subjected to qPCR to assess fold changes in gene expression levels. For qPCR reactions, the cDNA sample was mixed with TaqMan Fast Advanced Master Mix (Thermo Fisher Scientific), nuclease-free water (Invitrogen), and TaqMan assay primers, and the reaction was performed using a Bio-Rad CFX96 Real-Time PCR machine, following the manufacturer's instructions. The expression levels of the pluripotency markers NANOG (Hs02387400) and OCT3/4 (Hs04260367) were analyzed using commercially available TaqMan primers. ACTB (Hs01060665) was used as an internal control for

normalization. Gene expression levels were compared to those of non-encapsulated hMSCs, which were cultured under standard 2D conditions on a cell culture plate.

Immunostaining of hMSCs Cytoskeletal Organization: To examine the effects of HA-Cys and HA-Cys.KI hydrogels on the cytoskeletal organization (F-actin) of hMSCs, DAPI (6-diamidino-2-phenylindole dihydrochloride), and phalloidin staining (ThermoFisher) were used. hMSCs were encapsulated at a concentration of 1×10^6 cells mL^{-1} within the hydrogels and incubated at 37 °C for 5 days. After the incubation period, the hydrogels were washed twice with PBS and fixed with 4% paraformaldehyde for 30 min at room temperature. Cells were then permeabilized using 0.1% Triton X-100 (Sigma) for 20 min, followed by washing with PBS. To reduce nonspecific background staining, the samples were incubated in 0.5% bovine serum albumin (BSA) in PBS for 1 h. Following three washes with PBS, the cells were stained with DAPI (which labels cell nuclei) and rhodamine phalloidin (which selectively binds to F-actin filaments). Finally, the stained samples were visualized under a Zeiss LSM 700 confocal microscope using 10 \times and 63 \times objectives to assess cytoskeletal organization and morphology.

Printing: To evaluate the printability and cell-protection capabilities of the optimal hydrogel composition (HA-Cys + 50 mM KI), HA-Cys was dissolved in degassed PBS (2%, mentioned above) at pH \approx 5 to prevent disulfide formation. The pH was then adjusted to 7.4 after incorporating KI. To assess both the printability of the hydrogels containing cells and their ability to shield the encapsulated cells, C2812 chondrocyte cells and hMSCs were separately, and jointly, incorporated into the hydrogel matrix 45 min after pH adjustment. This mixture was subsequently loaded into a plastic printing cartridge from CELLINK Corporation, Sweden. Using a pneumatic printhead with a 30G needle (inner diameter of 159 μm) at a pressure of 250 kPa, various structures with rectilinear infill patterns were printed using a CELLINK BIO-X printer (CELLINK Corporation, Sweden). The printing process was conducted at intervals of 60, 90, 120, 150, and 180 min after pH adjustment, allowing the gel components laden with C2812 chondrocyte cells to optimize for printability. After printing, the structures were immersed in cell culture media. Cell distribution post-printing was visualized using Hoechst staining. Additionally, the precision of the printed structures compared to the original design was evaluated and measured the filament dimensions using microscopy images analyzed via ImageJ software. To explore the limitations of 3D bioprinting, structures with dimensions of 10 mm \times 10 mm \times 1 mm were printed using a 32G needle (inner diameter of 108 μm). The shape fidelity and filament dimensions were also assessed using microscopic images. Additionally, more complicated structures including a cube, cone, hollow cylinder, and a 50% simplified human ear were also printed using a 32G needle.

For visualization of separate and co-printing capabilities with C2812 chondrocyte cells and hMSCs, cells were pre-stained with nuclear markers Hoechst and SYTO 82 Orange, respectively. Predetermined structures were then printed, and fluorescent microscopy was used for imaging to assess the spatial distribution and compatibility of the two cell types. To determine the protective native of the hydrogel against anoikis, hydrogels with different cell types (C2812 and hMSCs) were prepared. These cell-laden hydrogels were extruded through a 32G needle at a constant pressure of 250 kPa. The extruded hydrogels were incubated for 1 and 3 days, after which the metabolic activity of the cells was assessed using the Presto Blue assay. Additionally, cell viability was evaluated using the Lactate Dehydrogenase (LDH) assay (Promega), a colorimetric method to quantify cytotoxicity following extrusion. The results were compared to those obtained from extruding cells suspended solely in cell culture media.

Cell-Interfaces Interactions—Migration of Chondrocyte and hMSCs in the Hydrogel: To evaluate the migration profiles of C2812 chondrocyte cells and hMSCs within a 3D hydrogel environment a 3D in vitro model was printed. First, hollow cylinders—either cell-free or cell-laden—were fabricated directly in a 96-well plate. Subsequently, the hollow inner region of these cylinders was filled with either cell-free or cell-laden hydrogel. After allowing the constructs to stabilize for 45–60 min, cell culture media was added to cover the structures, which were then incubated for real-time imaging at various time points. Before encapsulation in the hydrogels, C2812 chondrocytes and hMSCs were stained DiO and DiL (Vybrant

cell-labeling solutions, Thermo Fisher), respectively, to enable live imaging. Cell migration in the experiment was quantified using ImageJ software at each imaging time point.

Effect of Hydrogel Matrix and hMSCs on Inflammation-Stimulated Chondrocytes: C2812 chondrocytes were stimulated to adopt a pro-inflammatory phenotype by exposure to lipopolysaccharides (LPS, 5 $\mu\text{g mL}^{-1}$) for 24 h. A 3D bioprinting approach was employed to fabricate hollow cylindrical hydrogels composed of HA-Cys. In one experimental group, hMSCs were encapsulated within the hydrogel before printing. After the stabilization of the printed structures, the inner hollow space of the cell-free cylinders was filled with HA-Cys hydrogels containing different cellular configurations. These included: chondrocyte cells (control group), LPS-stimulated C2812 chondrocyte cells, and LPS-stimulated chondrocyte cells combined with KI. For the cylinders containing HA-Cys-encapsulated hMSCs, the inner hollow space was filled with hydrogels containing LPS-stimulated chondrocyte cells. Once the constructs were prepared, they were covered with cell culture media and incubated. After 3 days of incubation, the inner portions of the hydrogel constructs were collected using a biopsy punch. Cells were extracted from the gels through a combination of freezing and mechanical crushing. The isolated cells were lysed using a lysis buffer, and RNA extraction was performed using the RNeasy Plus Mini Kit (Qiagen) following the manufacturer's protocol. Subsequently, cDNA synthesis was carried out, and qPCR was conducted to assess gene expression levels. For qPCR, the cDNA samples were combined with TaqMan Fast Advanced Master Mix (Thermo Fisher Scientific), nuclease-free water (Invitrogen), and specific TaqMan assay primers. The reaction was run on a Bio-Rad CFX96 Real-time PCR machine following the manufacturer's instructions. The expression levels of the following genes were analyzed using commercially available TaqMan primers: TNF- α , IL-1 β , IL-6, IL-10, and TGF- β , and ACTB with ACTB serving as an internal control for normalization.

Statistical Analysis: All experiments were performed at least in triplicate. Statistical significance between groups in the various results was assessed using one-way and two-way ANOVA, conducted with GraphPad Prism Software (Version 8). A *p*-value of less than 0.05 ($P < 0.05$) was considered statistically significant for all tests. The significance levels were considered as follows: **** $P < 0.0001$, *** $P < 0.001$, ** $P < 0.01$, and * $P < 0.05$.

Supporting Information

Supporting Information is available from the Wiley Online Library or from the author.

Acknowledgements

Financial assistance for this research was provided by European Union's Horizon 2020 Marie Skłodowska-Curie H2020-MSCA-ITN-ETN-2020 (no. 955335), Swedish Strategic Research "StemTherapy" (Dnr 2009-1035), and the Swedish Research Council (Dnr 2020-04025). The authors thank Hamidreza Mokhtari for generously providing the authors with G-codes for 3D printing. The C2812 cells were a kind gift from Prof. Mary Goldring from Cell and Developmental Biology at Weill College Graduate School of Medical science, New York, United State, and Prof. Laura Creemers for shipping the cells. We also thank Prof. Martin Stoddart from the AO Foundation, Davos, Switzerland for providing hMSCs.

Conflict of Interest

The authors declare no conflict of interest.

Data Availability Statement

The data that support the findings of this study are available from the corresponding author upon reasonable request.

Keywords

bioinks, bioprinting, hyaluronic acid, hydrogels, in vitro models

Received: January 6, 2025

Revised: April 11, 2025

Published online:

-
- [1] Y. W. Ding, X. W. Zhang, C. H. Mi, X. Y. Qi, J. Zhou, D. X. Wei, *Smart Mater. Med.* **2023**, *4*, 59.
- [2] A. Munaz, R. K. Vadelu, J. St John, M. Barton, H. Kamble, N.-T. Nguyen, *J. Sci. Adv. Mater. Dev.* **2016**, *1*, 1.
- [3] S.-S. Yoo, *Expert Opin. Ther. Pat.* **2015**, *25*, 507.
- [4] P. Mancuso, S. Raman, A. Glynn, F. Barry, J. M. Murphy, *Front. Bioeng. Biotechnol.* **2019**, *7*, 9.
- [5] M. ter Huurne, R. Schelbergen, R. Blattes, A. Blom, W. de Munter, L. C. Grevers, J. Jeanson, D. Noël, L. Casteilla, C. Jorgensen, W. van den Berg, P. L. E. M. van Lent, *Arthritis Rheum.* **2012**, *64*, 3604.
- [6] Y. Liu, L. Lin, R. Zou, C. Wen, Z. Wang, F. Lin, *Cell Cycle* **2018**, *17*, 2411.
- [7] M. Maumus, C. Manferdini, K. Toupet, J.-A. Peyrafitte, R. Ferreira, A. Facchini, E. Gabusi, P. Bourin, C. Jorgensen, G. Lisignoli, D. Noël, *Stem Cell Res.* **2013**, *11*, 834.
- [8] J. Karvinen, M. Kellomäki, *Eur. Polym. J.* **2024**, *209*, 112864.
- [9] S. Liu, J.-M. Yu, Y.-C. Gan, X.-Z. Qiu, Z.-C. Gao, H. Wang, S.-X. Chen, Y. Xiong, G.-H. Liu, S.-E. Lin, A. McCarthy, J. V. John, D.-X. Wei, H.-H. Hou, *Mil. Med. Res.* **2023**, *10*, 16.
- [10] S. Tavakoli, A. Evans, O. P. Oommen, L. Creemers, J. B. Nandi, J. Hilborn, O. P. Varghese, *Mater. Today Bio* **2023**, *22*, 100768.
- [11] S. Wang, S. Tavakoli, R. P. Parvathaneni, G. N. Nawale, O. P. Oommen, J. Hilborn, O. P. Varghese, *Biomater. Sci.* **2022**, *1*, 6399.
- [12] H. Wang, S. C. Heilshorn, H. Wang, S. C. Heilshorn, *Adv. Mater.* **2015**, *27*, 3717.
- [13] S. Tavakoli, N. Krishnan, H. Mokhtari, O. P. Oommen, O. P. Varghese, *Adv. Funct. Mater.* **2024**, *34*, 2307040.
- [14] L. Bettanin, S. Saba, F. Z. Galetto, G. A. Mike, J. Rafique, A. L. Braga, *Tetrahedron Lett.* **2017**, *58*, 4713.
- [15] X. Z. Shu, Y. Liu, Y. Luo, M. C. Roberts, G. D. Prestwich, *Biomacromolecules* **2002**, *3*, 1304.
- [16] S. Chakravarthi, C. E. Jessop, N. J. Bulleid, *EMBO Rep.* **2006**, *7*, 271.
- [17] D. Bermejo-Velasco, A. Azémar, O. P. Oommen, J. Hilborn, O. P. Varghese, *Biomacromolecules* **2019**, *20*, 1412.
- [18] M. Kirihara, Y. Asai, S. Ogawa, T. Noguchi, A. Hatano, Y. Hirai, *Synthesis* **2007**, *21*, 3286.
- [19] L. Wang, L. Chen, Z. Qin, K. Ni, X. Li, Z. Yu, Z. Kuang, X. Qin, H. Duan, J. An, *Molecules* **2023**, *28*, 6789.
- [20] S. R. Ranamalla, S. Tavakoli, A. S. Porfire, L. R. Tefas, M. Banciu, I. Tomuța, O. P. Varghese, *Carbohydr. Polym.* **2024**, *339*, 122251.
- [21] J. W. Kuo, D. A. Swann, G. D. Prestwich, *Bioconjugate Chem.* **1991**, *2*, 232.
- [22] G. A. Bagiyani, I. K. Koroleva, N. V. Soroka, A. V. Ufimtsev, *Russ. Chem. Bull.* **2003**, *52*, 1135.
- [23] J. P. Danehy, B. T. Doherty, C. P. Egan, *J. Org. Chem.* **1971**, *36*, 2525.
- [24] M. I. González-Sánchez, E. Valero, R. G. Compton, *Sens. Actuators, B* **2016**, *236*, 1.
- [25] S. Wang, G. N. Nawale, O. P. Oommen, J. Hilborn, O. P. Varghese, *Polym. Chem.* **2019**, *10*, 4322.
- [26] S. Hayashi, S. Ishikawa, E. Ishii, M. Koike, T. Kaminaga, Y. Hamasaki, T. Sairenchi, G. Kobashi, K. Igawa, *J. Invest. Dermatol.* **2020**, *140*, 2001.
- [27] C. S. Bonnet, D. A. Walsh, *Rheumatology* **2005**, *44*, 7.
- [28] S. Briganti, M. Picardo, *J. Eur. Acad. Dermatol. Venereol.* **2003**, *17*, 663.
- [29] A. Blasi-Romero, C. Palo-Nieto, C. Sandström, J. Lindh, M. Strømme, N. Ferraz, *Polymers* **2021**, *13*, 249.
- [30] H. Jung, *Arch. Plast. Surg.* **2020**, *47*, 297.
- [31] F. L. C. Morgan, L. Moroni, M. B. Baker, *Adv. Healthcare Mater.* **2020**, *9*, 1901798.
- [32] M. Guvendiren, H. D. Lu, J. A. Burdick, *Soft Matter* **2012**, *8*, 260.
- [33] G. D. Nicodemus, S. J. Bryant, *Tissue Eng., Part B* **2008**, *14*, 149.
- [34] J. R. K. Samal, V. K. Rangasami, S. Samanta, O. P. Varghese, O. P. Oommen, *Adv. Healthcare Mater.* **2021**, *10*, 2002058.
- [35] J. Feng, K. Mineda, S. H. Wu, T. Mashiko, K. Doi, S. Kuno, K. Kinoshita, K. Kanayama, R. Asahi, A. Sunaga, K. Yoshimura, *Sci. Rep.* **2017**, *7*, 1548.
- [36] R. McBeath, D. M. Pirone, C. M. Nelson, K. Bhadriraju, C. S. Chen, *Dev. Cell* **2004**, *6*, 483.
- [37] D. Lü, C. Luo, C. Zhang, Z. Li, M. Long, *Biomaterials* **2014**, *35*, 3945.
- [38] H. Gerardo, A. Lima, J. Carvalho, J. R. D. Ramos, S. Couceiro, R. D. M. Travasso, R. Pires das Neves, M. Grãos, *Sci. Rep.* **2019**, *9*, 9086.
- [39] L. M. Marquardt, S. C. Heilshorn, *Curr. Stem Cell Rep.* **2016**, *2*, 207.
- [40] A. A. Foster, L. M. Marquardt, S. C. Heilshorn, *Curr. Opin. Chem. Eng.* **2017**, *15*, 15.
- [41] B. A. Aguado, W. Mulyasasmita, J. Su, K. J. Lampe, S. C. Heilshorn, *Tissue Eng., Part A* **2012**, *18*, 806.
- [42] X. Ma, J. Liu, W. Zhu, M. Tang, N. Lawrence, C. Yu, M. Gou, S. Chen, *Adv. Drug Delivery Rev.* **2018**, *132*, 235.
- [43] H. Le, W. Xu, X. Zhuang, F. Chang, Y. Wang, J. Ding, *J. Tissue Eng.* **2020**, *11*, 2041731420943839.
- [44] J. Rex, A. Lutz, L. E. Faletti, U. Albrecht, M. Thomas, J. G. Bode, C. Borner, O. Sawodny, I. Merfort, *Front. Physiol.* **2019**, *10*, 806.
- [45] A. Kulesza, L. Paczek, A. Burdzinska, *Biomedicines* **2023**, *11*, 445.
- [46] X. Yuan, T. M. Logan, T. Ma, *Front. Immunol.* **2019**, *10*, 977.